*Astronomy & Astrophysics* manuscript no. ngc3783_cos_preprint_102918
October 30, 2018


# HST/COS observations of the newly discovered obscuring outflow in NGC 3783

G.A. Kriss[1], M. Mehdipour[2], J.S. Kaastra[2,3], A. Rau[4], J. Bodensteiner[4,5], R. Plesha[1], N. Arav[6], E. Behar[7], S. Bianchi[8], G. Branduardi-Raymont[9], M. Cappi[10], E. Costantini[2], B. De Marco[11], L. Di Gesu[12], J. Ebrero[13], S. Kaspi[7], J. Mao[2,3], R. Middei[8], T. Miller[6], S. Paltani[12], U. Peretz[7], B.M. Peterson[1,14,15], P.-O. Petrucci[16], G. Ponti[4], F. Ursini[10], D.J. Walton[17], and X. Xu[6]

[1] Space Telescope Science Institute, 3700 San Martin Drive, Baltimore, MD 21218, USA
e-mail: gak@stsci.edu
[2] SRON Netherlands Institute for Space Research, Sorbonnelaan 2, 3584 CA Utrecht, the Netherlands
[3] Leiden Observatory, Leiden University, PO Box 9513, 2300 RA Leiden, the Netherlands
[4] Max-Planck-Institut für Extraterrestriche Physik, Gießenbachstraße, 85748, Garching, Germany
[5] Institute of Astronomy, KU Leuven, Celestijnenlaan 200D bus 2401, 3001 Leuven, BE
[6] Department of Physics, Virginia Tech, Blacksburg, VA 24061, USA
[7] Department of Physics, Technion-Israel Institute of Technology, 32000 Haifa, Israel
[8] Dipartimento di Matematica e Fisica, Università degli Studi Roma Tre, via della Vasca Navale 84, 00146 Roma, Italy
[9] Mullard Space Science Laboratory, University College London, Holmbury St. Mary, Dorking, Surrey, RH5 6NT, UK
[10] INAF-IASF Bologna, Via Gobetti 101, I-40129 Bologna, Italy
[11] Nicolaus Copernicus Astronomical Center, Polish Academy of Sciences, Bartycka 18, PL-00-716 Warsaw, Poland
[12] Department of Astronomy, University of Geneva, 16 Ch. d'Ecogia, 1290 Versoix, Switzerland
[13] European Space Astronomy Centre, P.O. Box 78, E-28691 Villanueva de la Cañada, Madrid, Spain
[14] Department of Astronomy, The Ohio State University, 140 West 18th Ave., Columbus, OH 43210, USA
[15] Center for Cosmology & AstroParticle Physics, The Ohio State University, 191 West Woodruff Ave., Columbus, OH 43210, USA
[16] Univ. Grenoble Alpes, CNRES, IPAG, 38000 Grenoble, France
[17] Institute of Astronomy, Madingley Road, CB3 0HA Cambridge, UK

Accepted, October 28, 2018

**ABSTRACT**

*Context.*
*Aims.* To understand the nature of transient obscuring outflows in active galactic nuclei, we use simultaneous multiwavelength observations with *XMM-Newton, NuSTAR*, the *Hubble Space Telescope* (HST), and the Max Planck Gesellschaft/European Southern Observatory (ESO) 2.2-m telescope triggered by soft X-ray absorption detected by *Swift*.
*Methods.* We obtained ultraviolet spectra on 2016 December 12 and 21 using the *Cosmic Origins Spectrograph* (COS) on HST simultaneously with X-ray spectra obtained with *XMM-Newton* and *NuSTAR*. We modeled the ultraviolet spectra to measure the strength and variability of the absorption, and used photoionization models to obtain its physical characteristics.
*Results.* We find new components of broad, blue-shifted absorption associated with Ly$\alpha$, N v, Si iv, and C iv in our COS spectra. The absorption extends from velocities near zero in the rest-frame of the host galaxy to $-6200$ km s$^{-1}$. These features appear for the first time in NGC 3783 at the same time as heavy soft X-ray absorption seen in the *XMM-Newton* X-ray spectra. The X-ray absorption has a column density of $\sim 10^{23}$ cm$^{-2}$, and it partially covers the X-ray continuum source. Combining the X-ray column densities with the UV spectral observations yields an ionization parameter for the obscuring gas of $\log \xi = 1.84^{+0.4}_{-0.2}$ erg cm s$^{-1}$. Despite the high intensity of the UV continuum in NGC 3783, F(1470 Å)=$8 \times 10^{-14}$ erg cm$^{-2}$ s$^{-1}$ Å$^{-1}$, the well known narrow UV absorption lines are deeper than in earlier observations in unobscured states, and low ionization states such as C iii appear, indicating that the narrow-line gas is more distant from the nucleus and is being shadowed by the gas producing the obscuration. Despite the high continuum flux levels in our observations of NGC 3783, moderate velocities in the UV broad line profiles have substantially diminished.
*Conclusions.* We suggest that a collapse of the broad line region has led to the outburst and triggered the obscuring event.

**Key words.** ultraviolet: galaxies – galaxies: active – galaxies: Seyfert – galaxies: individual: NGC 3783 – galaxies: absorption lines – galaxies: emission lines

## 1. Introduction

Outflows from active galactic nuclei (AGN) may be the regulating mechanism that links the growth of supermassive black holes at galaxy centers to the size of the host galaxy. A possible outcome of such a linkage is the correlation between central velocity dispersions in galaxies and the masses of their central black holes (Magorrian et al. 1998; Ferrarese & Merritt 2000; Gebhardt et al. 2000; Kormendy & Ho 2013). Feedback from outflows may also regulate the overall mass and size of the host galaxy (Silk & Rees 1998; King 2003; Ostriker et al. 2010; Soker 2010; Faucher-Giguère & Quataert 2012; Zubovas & Nayakshin 2014; Thompson et al. 2015).

AGN outflows manifest themselves in a variety of forms, from narrowly collimated radio jets to broad, wide-spread winds. In the latter case, these winds are often identified via their broad, blue-shifted absorption features in X-ray and ultraviolet spectra (Crenshaw et al. 2003), or extended, red and blue-shifted emission-line regions (Liu et al. 2013a,b, 2014). Again, the mechanisms for these various manifestations may vary, from radiatively driven (Murray & Chiang 1995, 1997; Proga et al. 2000; Thompson et al. 2015) or magnetically accelerated (Königl & Kartje 1994; Fukumura et al. 2010) winds originating from the accretion disk, or thermal winds originating either from the accretion disk, the broad-line region, or the obscuring torus (Krolik & Kriss 1995, 2001).

Understanding the physical properties of outflows to ascertain how they work is crucial for being able to model the interaction of central black holes with their host galaxies. Observationally, in the X-ray and the UV, outflows have appeared with a variety of characteristics, perhaps indicating several mechanisms may be at work. Examples include the X-ray warm absorbers and associated narrow UV absorption lines described by Crenshaw et al. (2003); ultra-fast outflows, typically only visible as broad, highly blue-shifted Fe K features (Pounds et al. 2003; Reeves et al. 2009; Tombesi et al. 2010; Nardini et al. 2015); and the newly discovered obscuring outflows showing strong soft X-ray absorption accompanied by broad, fast, blue-shifted UV absorption lines: NGC 5548 (Kaastra et al. 2014), Mrk 335 (Longinotti et al. 2013), NGC 985 (Ebrero et al. 2016), and most recently, NGC 3783 (Mehdipour et al. 2017).

In the case of obscuring outflows, the gas appears to be mildly ionized and has high column density ($10^{22} - 10^{23}$ cm$^{-2}$). This produces strong soft X-ray absorption, but no visible spectral features that allow diagnostics of the kinematics or ionization state of the gas. The crucial element in all the cases cited above is the availability of contemporaneous UV spectra. The UV absorption lines that appear in these events provide the necessary diagnostics that show gas outflowing (blue-shifted) with velocities and ionization states consistent with an origin in, or interior to the broad-line region (BLR). With no UV spectra, such obscuration events would be indistinguishable from other X-ray eclipsing events as studied by Markowitz et al. (2014), which could be caused just as easily by clouds in transverse motion as opposed to having a significant outflow component.

To understand the nature of obscuring outflows better and study their potential relationship to X-ray eclipsing events, we undertook a monitoring program with *Swift* (Gehrels et al. 2004) to find potential obscuring events that we could then study in detail with multiwavelength observations using *XMM-Newton* (Jansen et al. 2001), *NuSTAR* (Harrison et al. 2013), and the Cosmic Origins Spectrograph (COS) on the *Hubble Space Telescope (HST)*. Mehdipour et al. (2017) presented preliminary results from this campaign. They found that the obscuring gas has kinematics and physical characteristics comparable to gas normally associated with the BLR. Thus, further study of obscuring outflows may offer some insights into the physical structure of the BLR. Reverberation mapping (Blandford & McKee 1982; Peterson 1993) of the BLR has indicated that motions are consistent with Keplerian motion in a gravitational field dominated by the central black hole (Krolik et al. 1991; Peterson & Wandel 1999). Recent advances allowing two-dimensional reverberation mapping in both spatial and velocity dimensions (Horne et al. 2004; Bentz et al. 2010; Grier et al. 2013; Pancoast et al. 2014a,b) confirm the dominance of Keplerian motions, but also show evidence for inflows and outflows associated with the BLR. Models of accretion-disk winds have often suggested that the BLR may be an observational manifestation of such winds, either radiatively driven by line opacity (Murray & Chiang 1995, 1997; Proga et al. 2000; Thompson et al. 2015) or by radiation pressure on dust (Czerny & Hryniewicz 2011; Czerny et al. 2017; Baskin & Laor 2018), or magnetohydrodynamic (Königl & Kartje 1994; Fukumura et al. 2010). If obscuring outflows are related to such winds that produce the BLR, then their transient nature and its possible relationship to changes in the BLR may provide additional insights into how the BLR forms and evolves.

NGC 3783 has been studied extensively in past UV and X-ray observational campaigns. The reverberation mapping campaign using the *International Ultraviolet Explorer* (IUE) and ground-based observatories in 1991–1992 (Reichert et al. 1994; Stirpe et al. 1994) established the size of the broad-line region (BLR) at 4–10 lt-days based on the lags of prominent emission lines (Ly$\alpha$, C IV, Mg II, H$\beta$) relative to variations in the continuum emission. In 2000–2001 an intensive X-ray and UV monitoring campaign obtained many observations of NGC 3783 using *Chandra* (Kaspi et al. 2002), *HST* (Gabel et al. 2003a), and the *Far Ultraviolet Spectroscopic Explorer (FUSE)* (Gabel et al. 2003a). The high-resolution X-ray spectra revealed details of the X-ray warm absorber (Kaspi et al. 2002; Netzer et al. 2003) and its relationship to the narrow intrinsic absorption lines (Gabel et al. 2003a,b, 2005). The intrinsic UV absorption lines comprised four discrete components at outflow velocities ranging from $-1352$ to $-539$ km s$^{-1}$, and the ensemble closely matched the kinematic appearance of the X-ray absorption lines in the *Chandra* spectra (Gabel et al. 2003a). Their absorption depth displayed variations consistent with a photoionization response to changes in the UV continuum, and the density-sensitive C III* $\lambda$1176 multiplet yielded a density of log $n_e = 4.5$ cm$^{-3}$ for Component #1 ($v = -1311$ km s$^{-1}$), implying a distance of 25 pc for the gas producing the narrow UV absorption lines (Gabel et al. 2005). In contrast to the narrow UV absorption lines common in other Seyfert galaxies (Crenshaw et al. 2003), Component #1 has appeared to "decelerate", with its centroid evolving from an outflow velocity of $-1352$ km s$^{-1}$ to $-1043$ km s$^{-1}$ (Scott et al. 2014) over 14 years. This unusual kinematic behavior makes NGC 3783 an interesting object for continuing studies.

In this paper we describe the HST/COS observations and their analysis that were part of the detection of a new obscuring outflow in NGC 3783 by Mehdipour et al. (2017). In §2 we describe the UV and optical observations and our data reduction methods. In §3 we model the UV and optical spectra and present an analysis of the physical properties of the obscuring outflow and the evolution of the narrow intrinsic UV absorption lines over the past 15 years. §4 discusses the implications of our observations for the structure of the BLR and for the origin of the obscuring outflow and its potential influence on the host galaxy. §5 presents our conclusions.

## 2. Observations and Data Reduction

During *Swift* Cycle 12 in 2016 November, we detected spectral hardening in NGC 3783 indicative of an obscuring event. We triggered coordinated *XMM-Newton, NuSTAR*, and HST/COS observations on 2016-12-12 (Visit 3 in Program 14481) and 2016-12-21 (Visit 4). In addition, on 2016-12-12 we obtained ground-based spectroscopy of the H$\beta$ region using the Fiber-fed Extended Range Optical Spectrograph (FEROS) on the Max Planck Gesellschaft/European Southern Observatory (MPG/ESO) 2.2-m telescope. For a baseline spectral comparison to NGC 3783 in the unobscured state, we use archival *HST*

UV and optical spectra obtained with the Space Telescope Imaging Spectrograph (STIS) (Woodgate et al. 1998).

### 2.1. COS Observations

Each COS observation consisted of a two-orbit visit using gratings G130M and G160M to cover the 1130–1800 Å wavelength range at a resolving power of ∼15,000 (Green et al. 2012). We used multiple central wavelength settings and multiple FP-POS positions to cover the gaps between detectors A and B for each grating, and to sample the spectrum on different sections of each detector to allow for removal of detector artifacts and other flat-field anomalies. Table 1 provides a summary of the various COS exposures.

Using updated wavelength calibrations, flat fields, and flux calibrations, we reprocessed our individual exposures as described by Kriss et al. (2011) and De Rosa et al. (2015). We then cross-correlated each exposure with prior HST/STIS observations of NGC 3783 (Gabel et al. 2003a) to adjust the zero-points of their wavelength scales before combining them into merged spectra representing each visit, and the two 2016 visits combined. Figure 1 shows the full merged spectrum from both 2016 visits. Since NGC 3783 was exceptionally bright during both of our visits (mean flux F(1470 Å) = $7.6 \times 10^{-14}$ erg cm$^{-2}$ s$^{-1}$ Å$^{-1}$ compared to the historical average of $5.0 \times 10^{-14}$ erg cm$^{-2}$ s$^{-1}$ Å$^{-1}$ (Dunn et al. 2006)), each merged spectrum achieves a signal-to-noise (S/N) ratio exceeding 40 per resolution element over the wavelength range from Ly$\alpha$ to the C IV line.

### 2.2. FEROS Observations

We observed NGC 3783 with the Fibre-fed Extended Range Optical Spectrograph (Kaufer et al. 1999, FEROS) at the MPG/ESO 2.2-m telescope at the ESO La Silla Observatory. Our spectra covered the wavelength range 3500–9200 Å at a resolving power of 48,000. Starting at 07:36 GMT on 2016-12-12, three 10 minute exposures were performed successively. Wavelength calibration frames were obtained with ThArNe lamps.

The FEROS spectra were reduced manually using the standard pipeline (FEROS-DRS[1]) based on ESO-MIDAS. Before the actual data reduction, the three exposures were averaged and a cosmic ray rejection was performed. The successive data reduction included flat fielding, bias and background subtraction, and wavelength calibration.

### 2.3. Archival HST Data

In 2000–2001 an intensive X-ray and UV monitoring campaign obtained many observations of NGC 3783 using *Chandra* (Kaspi et al. 2002), *HST* (Gabel et al. 2003a), and the *Far Ultraviolet Spectroscopic Explorer (FUSE)* (Gabel et al. 2003a). We obtained the calibrated STIS spectra from the Mikulski Archive for Space Telescopes (MAST) and combined them as an unweighted average to use as our baseline for comparison of the new COS spectra.

In 2011, HST program 12212 (PI: M. Crenshaw) obtained an optical long-slit spectrum of the nuclear region of NGC 3783 using the STIS CCD, grating G430M, and the 52×0.2″ slit. This spectrum covers the wavelength region surrounding H$\beta$ and [O III], and we use it as our baseline for comparing our ground-based spectrum in the obscured state to an unobscured state. Table 1 gives the observational details for these spectra. The STIS spectra were taken at three dithered slit positions to facilitate removal of cosmic rays and defective pixels. After correcting the data for charge-transfer inefficiency using a pixel-based algorithm based on Anderson & Bedin (2010), we shifted the calibrated two-dimensional images to a common geometric position using integer-pixel shifts and combined them using a median filter to reject bad pixels. After this process, some cosmic ray residuals were still present. We identified these interactively, and interpolated across them using the fluxes in the adjacent pixels.

## 3. Data Analysis

The absorption in the blue wings of the Ly$\alpha$, N V, Si IV, and C IV emission lines in NGC 3783 is difficult to discern on the scale of Figure 1, but it is more readily apparent in Figure 3 of Mehdipour et al. (2017), where one can compare it directly to the high-quality STIS spectrum obtained in 2001 (Gabel et al. 2003a) during an unobscured epoch. To quantitatively assess the properties of the obscuration that appears in the COS spectrum, we start with a model of the emission lines and continuum based on the 2001 STIS spectrum. Our model is similar to the comprehensive model used for NGC 5548 (Kaastra et al. 2014) and consists of a power law continuum, $F_\lambda = F_{1000\text{Å}}(\lambda/1000\text{Å})^{-\alpha}$, that is reddened by fixed extinction of E(B-V)=0.107 (Schlafly & Finkbeiner 2011), and Gaussian emission components for each significant emission line. As usual, the bright components require several Gaussians. Ly$\alpha$ and C IV are each comprised of 4 Gaussians: a narrow component with full-width at half-maximum (FWHM) ∼ 900 km s$^{-1}$, a medium-broad component (FWHM ∼ 2500 km s$^{-1}$), a broad component (FWHM ∼ 4500 km s$^{-1}$), and a very broad component (FWHM ∼ 10,000 km s$^{-1}$). N V, Si IV and He II require only three components (narrow, medium broad or broad, and very broad), and the weaker lines usually require only a broad component, or a narrow plus a medium-broad to broad. For N V, Si IV, and C IV, we allow for both lines in the doublets for the narrow, medium-broad, and broad components, but only assume one component for the very broad line. We also assume the doublets are optically thick and have flux ratios of 1:1. The whole emission model is then absorbed by foreground Galactic H I Ly$\alpha$ as a damped Lorentzian profile with column density N(HI)=$9.59 \times 10^{20}$ cm$^{-2}$ (Murphy et al. 1996).

We note that this Gaussian decomposition is a semi-empirical model and that the individual components do not necessarily represent physically distinct portions of the line-emitting regions. They also are neither independent nor orthogonal. However, in both NGC 5548 and NGC 3783, there are distinct narrow portions of the line profile that are stable over time in both width, velocity, and flux (Crenshaw et al. 2009). As we show later, the narrow-line components in the spectra at all epochs vary by $\lesssim 10\%$. The lack of variability implies that these narrow components are likely representative of emission from the narrow-line region at some distance (∼1 pc) from the nucleus. This is important since these narrow components are probably not absorbed by the obscurer.

We optimize parameters for each component in the model using the spectral fitting program `specfit` (Kriss 1994) in IRAF. The wavelength regions for our fits exclude all absorption lines, both intrinsic to NGC 3783, and the foreground lines from the interstellar medium (ISM). Since the intrinsic absorbers affect significant portions of the blue sides of all the lines, best-fit parameters are largely (but not exclusively) determined by the red sides

[1] https://www.eso.org/sci/facilities/lasilla/instruments/feros/tools/drs.html

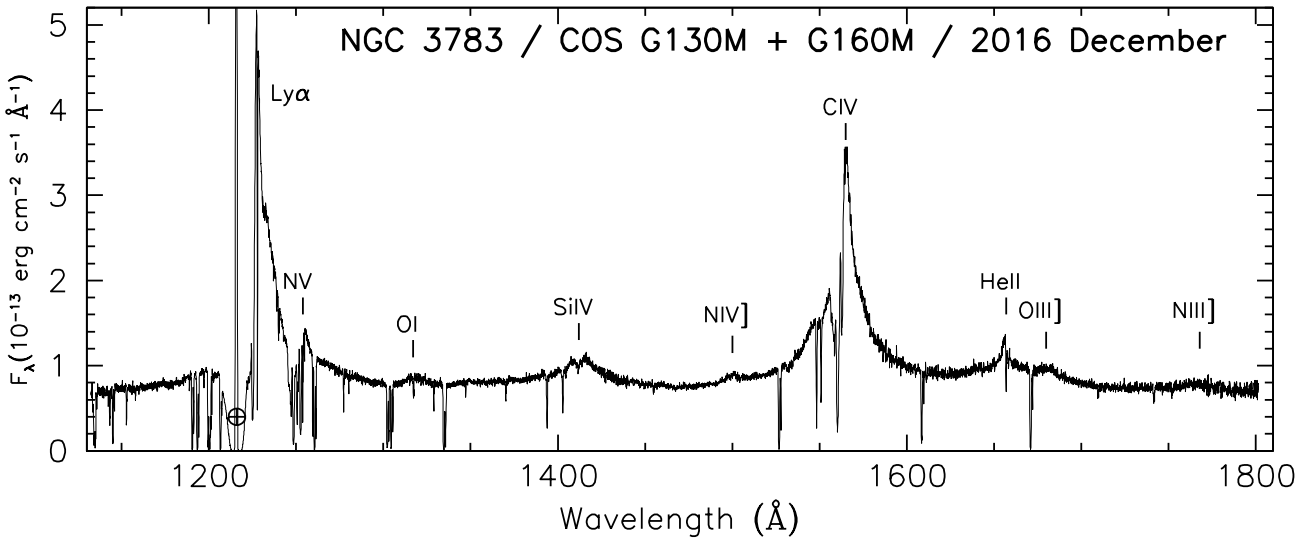


**Fig. 1.** Calibrated and merged COS spectrum of NGC 3783 from 2016 December. Data are binned by 8 pixels, or approximately one resolution element. We label the most prominent emission features. Geocoronal emission in the center of the Milky Way Ly$\alpha$ absorption trough is indicated with an Earth symbol.

of the profiles and the line wings (> 1500 km s$^{-1}$ from line center for the STIS spectrum, and > 6500 km s$^{-1}$ for the 2016 COS spectra). For each spectrum, we optimize our fit in stages. The continuum normalization and power-law index are initially fixed using continuum regions near the blue and red ends of the spectrum. We initially fix the line centers at the host galaxy systemic velocity, z=0.00973, a value determined via H I 21-cm measurements (Theureau et al. 1998). We interactively choose widths and fluxes for the lines that fit well by eye. Next, we let all the emission line fluxes vary. Once these have converged, we let the continuum parameters also vary freely to optimize its shape simultaneously with the broad wings of the emission lines. At this point the fit bears a good resemblance to the actual spectrum, but is not a good match in all details. To approach full convergence, we then successively address the major emission-line regions independently, as described below. For these individual regions, we freeze the continuum parameters, free the line widths and fluxes first, and finally the line centers. Since the line centers, widths, and fluxes are free, we are not forcing any assumptions of symmetry on the line profiles; slight asymmetries in the line profiles can be accommodated by the differing centroids and widths of the various components. Once the major line-emitting regions have been fit (Ly$\alpha$+N v, Si IV, C IV, and He II), we let all parameters vary freely to converge to a globally optimized best fit.

In the sections below we separately describe in further detail our fitting process for the STIS 2001 spectrum first, and then the COS 2016 spectra.

### *3.1. Modeling the Unobscured STIS Spectrum of NGC 3783*

To model the COS spectra of NGC 3783, we establish a baseline model by fitting the average STIS spectrum accumulated in the monitoring campaign from 2000–2001 that included STIS, *FUSE*, and *Chandra* observations (Gabel et al. 2003a; Kaspi et al. 2002). This spectrum has high S/N, and modeling it is straightforward, especially for C IV, since much of the line profile is uncontaminated by absorption. In this spectrum, after establishing preliminary continuum and line fluxes, we then fit the C IV profile in detail. This is the least-blended, highest S/N ratio emission feature. The complement of Gaussian widths and relative fluxes here serve as a starting point for the other major features. We then fit the Ly$\alpha$+N v region, followed by Si IV and He II. After all regions have been individually optimized, we iterate on the final model of the full spectrum to obtain the best fit. The best-fit emission-line properties are given in Table 2.

#### 3.1.1. Modeling the Unobscured C IV Profile

Figure 2 shows the best fit, with the profiles of all the C IV emission components shown as well as the continuum level. (Note that the best fit shown here is the final result following the global optimization to the full spectrum after all regions have been separately fit.) The C IV narrow-line emission (cyan) is slightly blueshifted by about −265 km s$^{-1}$. The medium-broad emission (blue) and the very broad emission (magenta) lie near the systemic velocity. The broad components of the line profile (green) have a significant blue shift of −900 km s$^{-1}$.

#### 3.1.2. Modeling the Unobscured Ly$\alpha$ Profile

The Ly$\alpha$+N v region is more complicated due to the blending of the Ly$\alpha$ and N v profiles and the strong impact of damped Ly$\alpha$ absorption from the Milky Way. Although we use the C IV profile as a guide and choose initial values for the Ly$\alpha$ components based on the C IV best fit, we do not constrain or tie these components to those determined for C IV. The final results do not wander far from these initial guesses, but we note that trial attempts with different plausible initial conditions also result in good fits that are slightly different; the blending and the foreground damped absorption lead to fits that are highly degenerate. Figure 3 illustrates the final fit to this region. As for C IV, the narrow-line emission is significantly blue shifted, with a peak at −340 km s$^{-1}$. The medium-broad emission is also blueshifted at −250 km s$^{-1}$. In contrast to C IV, the broad emission here is red-

**Table 1.** UV and Optical Observations of NGC 3783

| Data Set Name | Date | Start Time (GMT) | Start Time (MJD) | Exposure Time (s) | Grating/Tilt/FP-POS |
|---|---|---|---|---|---|
| obgu03010 | 2011-03-23 | 19:41:12 | 55643.820286 | 696 | STIS/CCD/G430M |
| obgu03020 | 2011-03-23 | 19:53:58 | 55643.829152 | 696 | STIS/CCD/G430M |
| obgu03030 | 2011-03-23 | 21:11:46 | 55643.883179 | 696 | STIS/CCD/G430M |
| lbgu19010 | 2011-05-26 | 10:40:51 | 55707.445041 | 481 | G130M/1291/3 |
| lbgu19020 | 2011-05-26 | 10:52:19 | 55707.452998 | 481 | G130M/1300/3 |
| lbgu19030 | 2011-05-26 | 11:03:47 | 55707.460961 | 481 | G130M/1309/3 |
| lbgu19040 | 2011-05-26 | 12:05:01 | 55707.503484 | 481 | G130M/1318/3 |
| lbgu19050 | 2011-05-26 | 12:17:11 | 55707.511933 | 2425 | G160M/1589/3 |
| lbgu19060 | 2011-05-26 | 12:30:34 | 55707.521227 | 2425 | G160M/1600/3 |
| lbgu19070 | 2011-05-26 | 13:46:04 | 55707.573657 | 2425 | G160M/1611/3 |
| lbgu19080 | 2011-05-26 | 13:59:27 | 55707.582951 | 2425 | G160M/1623/3 |
| lc3x01010 | 2013-03-30 | 14:48:30 | 56381.617014 | 460 | G130M/1291/3 |
| lc3x01020 | 2013-03-30 | 14:59:23 | 56381.624572 | 460 | G130M/1300/3 |
| lc3x01030 | 2013-03-30 | 15:52:17 | 56381.661308 | 460 | G130M/1309/3 |
| lc3x01040 | 2013-03-30 | 16:03:10 | 56381.668866 | 340 | G130M/1318/3 |
| lc3x01050 | 2013-03-30 | 16:13:24 | 56381.675983 | 580 | G160M/1589/3 |
| lc3x01060 | 2013-03-30 | 16:26:08 | 56381.684815 | 580 | G160M/1600/3 |
| lc3x01070 | 2013-03-30 | 17:28:05 | 56381.727836 | 580 | G160M/1611/3 |
| lc3x01080 | 2013-03-30 | 17:40:49 | 56381.736678 | 424 | G160M/1623/3 |
| FEROS | 2016-12-12 | 07:36:00 | 57734.316667 | 1800 | FEROS |
| ld3e03kgq[a] | 2016-12-12 | 12:13:56 | 57734.509676 | 475 | G130M/1291/3 |
| ld3e03kkq | 2016-12-12 | 12:23:55 | 57734.516609 | 475 | G130M/1291/4 |
| ld3e03kmq | 2016-12-12 | 12:35:16 | 57734.524502 | 455 | G130M/1327/1 |
| ld3e03koq | 2016-12-12 | 12:44:56 | 57734.531204 | 455 | G130M/1327/2 |
| ld3e03kyq | 2016-12-12 | 13:38:36 | 57734.568472 | 564 | G160M/1600/3 |
| ld3e03l2q | 2016-12-12 | 13:50:04 | 57734.576436 | 564 | G160M/1600/4 |
| ld3e03l4q | 2016-12-12 | 14:02:48 | 57734.585278 | 564 | G160M/1623/1 |
| ld3e03l6q | 2016-12-12 | 14:14:16 | 57734.593241 | 564 | G160M/1623/2 |
| ld3e04pmq[a] | 2016-12-21 | 15:25:00 | 57743.642361 | 475 | G130M/1291/3 |
| ld3e04poq | 2016-12-21 | 15:34:59 | 57743.649294 | 475 | G130M/1291/4 |
| ld3e04pqq | 2016-12-21 | 15:46:20 | 57743.657187 | 455 | G130M/1327/1 |
| ld3e04psq | 2016-12-21 | 15:56:00 | 57743.663889 | 455 | G130M/1327/2 |
| ld3e04puq | 2016-12-21 | 16:07:43 | 57743.672026 | 564 | G160M/1600/3 |
| ld3e04pwq | 2016-12-21 | 17:00:22 | 57743.708588 | 564 | G160M/1600/4 |
| ld3e04pyq | 2016-12-21 | 17:13:06 | 57743.717431 | 564 | G160M/1623/1 |
| ld3e04q0q | 2016-12-21 | 17:24:34 | 57743.725394 | 564 | G160M/1623/2 |

**Notes.**
[a] We collectively refer to the visits on 2016-12-12 as Visit 3, or "v3".
[b] We collectively refer to the visits on 2016-12-21 as Visit 4, or "v4".

shifted to +350 km s$^{-1}$ (for both Ly$\alpha$ and N v), but this may well be biased because of the lack of a good view of the blue wing of Ly$\alpha$ and the blending of N v with Ly$\alpha$.

### 3.1.3. Modeling the Unobscured Si IV Profile

Fitting the Si IV region is simpler since there is less contaminating intrinsic and foreground absorption. The line is fainter, however, and the S/N is not as good as in the C IV and Ly$\alpha$ regions. Therefore an adequate fit requires only two narrow and two broad components for the Si IV doublets, and a single very broad Si IV base. Si IV is also blended with several O IV] transitions; however, these appear to be weak, and only the cluster of the strongest transitions at $\lambda$1401 is included in our model as an additional narrow component. The best fit is shown in Figure 4. As with C IV and Ly$\alpha$, the narrow lines are slightly blue shifted at −100 km s$^{-1}$, and, similar to Ly$\alpha$, the broad lines are slightly redshifted at +120 km s$^{-1}$.

### 3.1.4. Modeling the Unobscured He II Profile

Finally, we show the fit to the He II region. This is important for establishing a good template for the broad-line region since He II $\lambda$1640 is a recombination line to the excited n=2 state, and therefore unlikely to be affected by absorption.[2] It is also similar in ionization to C IV, and should form in the same physical regions and have similar overall kinematics. Since He II emission is faint, like Si IV, only three components are required: a narrow, a broad,

[2] He II n=2 is 48 eV above the ground state, and maintaining a significant population of ions in this state requires high temperatures (T $\gtrsim 6 \times 10^5$ K), or high densities (n $\gtrsim 10^{15}$ cm$^{-3}$) neither of which are typical of BLR conditions of T $\sim 10^4$ K and n $\sim 10^{10}$ cm$^{-3}$ (Osterbrock & Ferland 2006).

**Table 2.** Emission-Line Parameters for the STIS 2000–2001 and COS 2016 Spectra of NGC 3783

| | | STIS 2000–2001 | | | COS 2016 | | |
|---|---|---|---|---|---|---|---|
| Feature | $\lambda_0^a$ | Flux[b] | $v_{sys}^c$ | FWHM[d] | Flux[b] | $v_{sys}^c$ | FWHM[d] |
| C III | 1176.01 | 1.1 ± 0.4 | −100 ± 70 | 1330 ± 170 | 40.0 ± 4.4 | 150 ± 20 | 1510 ± 50 |
| Ly$\alpha$ | 1215.67 | 84.0 ± 2.7 | −40 ± 20 | 800 ± 30 | 100.0 ± 3.8 | −40 ± 20 | 800 ± 20 |
| Ly$\alpha$ | 1215.67 | 240.0 ± 9.6 | 40 ± 30 | 2500 ± 20 | 270.0 ± 8.1 | 40 ± 30 | 2500 ± 30 |
| Ly$\alpha$ | 1215.67 | 120.0 ± 4.6 | 670 ± 50 | 5550 ± 40 | 290.0 ± 9.7 | 850 ± 30 | 6330 ± 30 |
| Ly$\alpha$ | 1215.67 | 300.0 ± 9.8 | −270 ± 30 | 14940 ± 100 | 400.0 ± 13.0 | 150 ± 40 | 15960 ± 60 |
| N v blue | 1238.82 | 6.4 ± 0.2 | −40 ± 20 | 980 ± 20 | 7.6 ± 0.3 | −40 ± 30 | 980 ± 60 |
| N v red | 1242.80 | 6.4 ± 0.2 | −40 ± 20 | 980 ± 20 | 7.6 ± 0.3 | −40 ± 30 | 980 ± 20 |
| N v blue | 1238.82 | 13.0 ± 0.7 | 350 ± 40 | 2850 ± 40 | 1.6 ± 0.3 | 350 ± 70 | 2850 ± 120 |
| N v red | 1242.80 | 13.0 ± 0.7 | 350 ± 40 | 2850 ± 40 | 1.6 ± 0.3 | 350 ± 70 | 2850 ± 120 |
| N v | 1240.89 | 40.0 ± 1.6 | 660 ± 60 | 10380 ± 180 | 28.0 ± 2.9 | 1410 ± 140 | 12140 ± 140 |
| Si II | 1260.42 | 1.7 ± 0.1 | −150 ± 20 | 1600 ± 20 | 1.5 ± 0.2 | −150 ± 50 | 1600 ± 50 |
| O I+Si II | 1304.46 | 20.0 ± 0.8 | 0 ± 30 | 3460 ± 40 | 11.0 ± 1.1 | 220 ± 50 | 2500 ± 40 |
| C II | 1334.34 | 9.6 ± 0.3 | 0 ± 50 | 3460 ± 40 | 3.1 ± 0.1 | 110 ± 40 | 2500 ± 20 |
| Si IV blue | 1393.76 | 8.3 ± 0.3 | −90 ± 20 | 1640 ± 30 | 4.3 ± 0.3 | −280 ± 50 | 1170 ± 70 |
| Si IV red | 1402.77 | 8.3 ± 0.3 | −90 ± 20 | 1640 ± 30 | 4.3 ± 0.3 | −280 ± 50 | 1170 ± 20 |
| Si IV blue | 1393.76 | 23.0 ± 0.7 | 120 ± 20 | 4460 ± 30 | 23.0 ± 0.9 | −270 ± 30 | 5160 ± 60 |
| Si IV red | 1402.77 | 23.0 ± 0.7 | 120 ± 20 | 4460 ± 30 | 23.0 ± 0.9 | −270 ± 30 | 5160 ± 20 |
| Si IV | 1398.19 | 63.0 ± 1.9 | −1170 ± 30 | 12410 ± 80 | 55.0 ± 2.3 | −2730 ± 40 | 13480 ± 290 |
| O IV] | 1400.37 | 5.2 ± 0.4 | 0 ± 20 | 1640 ± 80 | 0.8 ± 0.1 | 900 ± 60 | 1170 ± 20 |
| O IV] | 1400.37 | ... | ... | ... | 9.1 ± 0.5 | 900 ± 60 | 5160 ± 20 |
| N IV] | 1485.80 | 14.0 ± 0.5 | −10 ± 40 | 2600 ± 40 | 2.9 ± 0.4 | −130 ± 80 | 1170 ± 20 |
| N IV] | 14z5.80 | ... | ... | ... | 8.3 ± 0.4 | −130 ± 80 | 3250 ± 20 |
| C IV blue | 1548.19 | 40.0 ± 1.7 | −60 ± 20 | 940 ± 40 | 36.0 ± 1.7 | −60 ± 30 | 940 ± 30 |
| C IV red | 1550.77 | 40.0 ± 1.7 | −60 ± 20 | 940 ± 40 | 36.0 ± 1.7 | −60 ± 30 | 940 ± 20 |
| C IV blue | 1548.19 | 80.0 ± 2.6 | 140 ± 20 | 2840 ± 20 | 2.3 ± 0.6 | 140 ± 20 | 2840 ± 20 |
| C IV red | 1550.77 | 80.0 ± 2.6 | 140 ± 20 | 2840 ± 20 | 2.3 ± 0.6 | 140 ± 20 | 2840 ± 20 |
| C IV blue | 1548.19 | 84.0 ± 2.7 | −950 ± 20 | 4580 ± 30 | 180.0 ± 5.5 | −710 ± 30 | 4640 ± 30 |
| C IV red | 1550.77 | 84.0 ± 2.7 | −950 ± 20 | 4580 ± 30 | 180.0 ± 5.5 | −710 ± 30 | 4640 ± 30 |
| C IV | 1549.48 | 310.0 ± 9.3 | −60 ± 20 | 10030 ± 30 | 340.0 ± 11.0 | −70 ± 30 | 12710 ± 40 |
| He II | 1640.45 | 13.0 ± 0.5 | −140 ± 20 | 990 ± 20 | 14.0 ± 0.6 | 10 ± 50 | 820 ± 30 |
| He II | 1640.45 | 9.2 ± 0.3 | −510 ± 40 | 3000 ± 100 | 7.6 ± 1.2 | 1250 ± 40 | 3990 ± 900 |
| He II | 1640.45 | 140.0 ± 4.4 | −470 ± 30 | 11280 ± 30 | 160.0 ± 6.3 | −120 ± 30 | 12460 ± 50 |
| O III] | 1659.85 | 3.6 ± 0.2 | 0 ± 50 | 1200 ± 100 | 3.1 ± 0.4 | 150 ± 40 | 1210 ± 30 |
| O III] | 1665.19 | 7.6 ± 0.6 | 0 ± 10 | 1200 ± 100 | 5.7 ± 0.4 | 150 ± 20 | 1210 ± 20 |
| N III] | 1750.00 | ... | ... | ... | 21.0 ± 0.7 | 0 ± 30 | 3270 ± 40 |

**Notes.**

[a] Vacuum rest wavelength of the spectral feature (Å).

[b] Integrated flux in units of $10^{-14}$ erg cm$^{-2}$ s$^{-1}$.

[c] Velocity (in km s$^{-1}$) relative to a systemic redshift of z = 0.00973 (Theureau et al. 1998).

[d] Full-width at half-maximum (km s$^{-1}$).

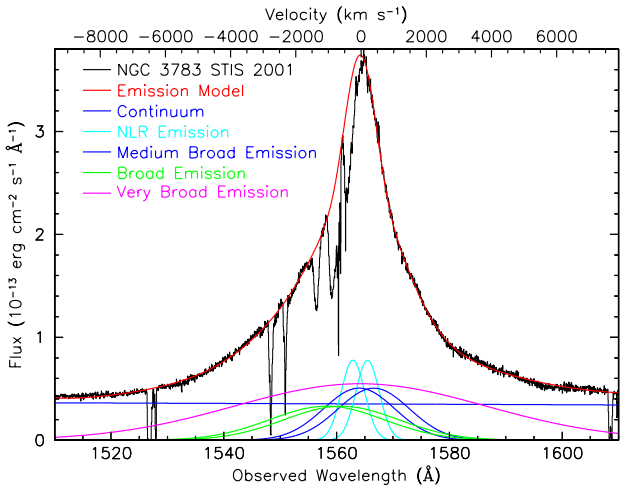


**Fig. 2.** Average STIS spectrum of the C IV region from all observations in the 2000–2001 campaign re-binned into 0.05 Å pixels (black histogram). The solid red line tracing the data is the total emission model. The key in the figure identifies the emission components in our model. The velocity scale along the top axis is for the blue component of the C IV doublet, $\lambda$1548.195, relative to the host galaxy systemic redshift, z=0.00973 (Theureau et al. 1998).

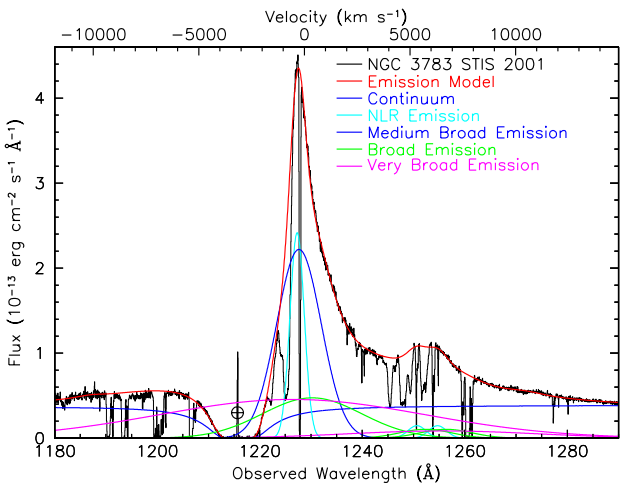


**Fig. 3.** Average STIS spectrum of the Ly$\alpha$+N V region from all observations in the 2000–2001 campaign re-binned into 0.05 Å pixels (black histogram). The solid red line tracing the data is the total emission model. The key in the figure identifies the emission components in our model. The velocity scale along the top axis is for Ly$\alpha$ $\lambda$1215.67, relative to the host galaxy systemic redshift, z=0.00973 (Theureau et al. 1998). Geocoronal emission in the center of the Milky Way Ly$\alpha$ absorption trough is indicated with an Earth symbol. The solid blue line showing the continuum also illustrates the impact of the damped Milky Way Ly$\alpha$ absorption. Note that the influence of this damping profile extends all the way from 1180 Å on through the peak of Ly$\alpha$ in NGC 3783 and into the N V profile at 1250 Å.

and a very broad component. There is also slight contamination on the red wing by two O III] transitions, which we model with individual narrow components. Also note that the red half of the line center is strongly absorbed by foreground interstellar Al II $\lambda$1670. Finally, this whole complex sits atop the far red wing of the much brighter C IV emission line. Figure 5 shows the best fit to the He II region. As for all previous emission lines, the narrow-line component is slightly blue-shifted at −150 km s$^{-1}$; the broad

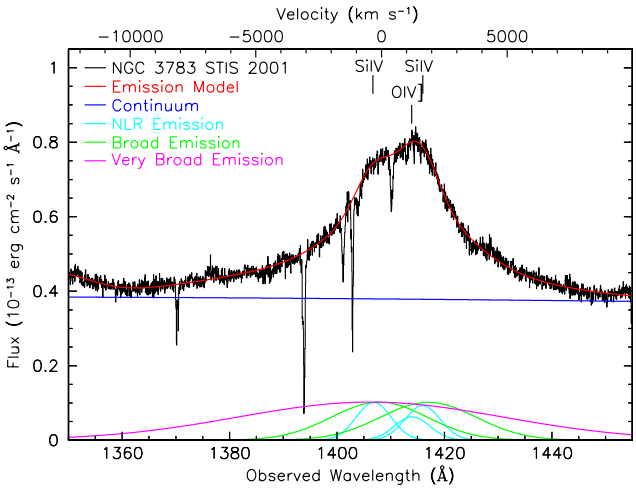


**Fig. 4.** Average STIS spectrum of the Si IV region from all observations in the 2000–2001 campaign re-binned into 0.05 Å pixels (black histogram). The solid red line tracing the data is the total emission model. The key in the figure identifies the emission components in our model. The velocity scale along the top axis is for Si IV $\lambda$1393.755, relative to the host galaxy systemic redshift, z=0.00973 (Theureau et al. 1998).

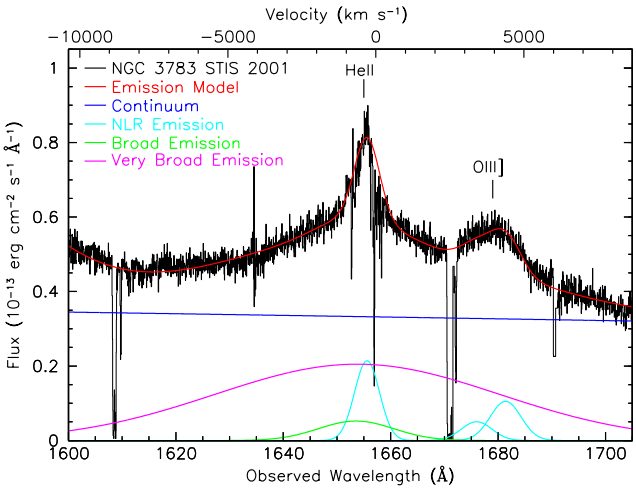


**Fig. 5.** Average STIS spectrum of the He II region from all observations in the 2000–2001 campaign re-binned into 0.05 Å pixels (black histogram). The solid red line tracing the data is the total emission model. The key in the figure identifies the emission components in our model. The velocity scale along the top axis is for He II $\lambda$1640.45, relative to the host galaxy systemic redshift, z=0.00973 (Theureau et al. 1998). All narrow absorption features are foreground ISM lines.

component is significantly blue-shifted at −520 km s$^{-1}$, but not as strongly as C IV.

### 3.2. Modeling the Average Obscured COS Spectrum of NGC 3783

Now that we have a good baseline model for the emission spectrum of NGC 3783, we can look at how the spectrum has changed from the unobscured state in 2001 to the obscured state that appears in our 2016 observation. We first fit the unweighted average sum of the two spectra from 2016-12-12 and 2016-21-21. As for the STIS spectrum, we fit the obscured COS selected regions at a time, beginning with He II, which we do not expect to be absorbed, followed by C IV, Ly$\alpha$+N V, and then Si IV. Af-

ter all regions have been individually optimized, we iterate on the final model of the full spectrum to obtain the best fit. Table 2 compares the best-fit emission-line properties for the average obscured COS spectrum in 2016 to the STIS spectrum from 2000–2001. Once we have this fit to the average spectrum, we then scale the model to adjust the continuum and line fluxes to the levels of the individual observations on 2016-12-12 and 2016-12-21, and then optimize the fits to each of these individual spectra. Results for the two separate observations are given in Table 3. In the following sections, we describe the fits to each of the individual regions in the obscured COS spectrum.

### 3.2.1. Modeling the Obscured He II Profile

Since we do not expect the He II emission line to be absorbed, we begin our fits with that line to see what intrinsic changes in the profile of the broad emission lines may have taken place between 2001 and 2016. Figure 6 compares the STIS 2001 spectrum to the COS 2016 spectrum. The continuum and the underlying emission of the C IV profile have been subtracted. The STIS spectrum is scaled up by a factor of 1.2 to match the flux in the high-velocity wings. O III] emission that sits on the red wing of He II has not been removed. One can see that overall, there is little change in the He II profile. Interestingly, the narrow component has moved redward and now lies at the systemic velocity. To optimize the model to the COS spectrum, we adjust the line fluxes in the model and the wavelength of the narrow component accordingly before letting the fit iterate to a new minimum. The resulting best fit is shown in Figure 6.

To compare the broad-line region profiles more closely, we subtract the modeled narrow emission lines from each profile and show the result in Figure 7. Here you can see that the STIS and COS profiles are very similar, except for a little added emission in the STIS spectrum on the blue side of line center. Although the STIS spectrum exhibits this excess emission relative to COS, there is no indication of broad absorption in the COS spectrum; the differences between the two profiles are accommodated merely by adjusting the flux and wavelength of the broad component (now shifted to the red as for the narrow component). Table 2 shows that the flux in the broad component of the COS spectrum is 17% lower compared to STIS, and shifted 1760 km s$^{-1}$ (10 Å) to the red. The fitted line profile passes smoothly through all the data in both line wings.

### 3.2.2. Modeling the Obscured C IV Profile

From our fit to the He II profile, we expect that our basic model for C IV should also be very similar in the COS 2016 spectrum compared to the STIS 2001 spectrum. Figure 8 compares the C IV profile from STIS 2001 to COS 2016. As for He II, both spectra have been continuum subtracted, and the STIS spectrum has been scaled up by a factor of 1.45 so that the intensities match in the broad wings beyond ±6000 km s$^{-1}$. For reference, for COS 2016 the continuum flux F(1560Å)=7.5 × 10$^{-14}$ erg cm$^{-2}$ s$^{-1}$ Å$^{-1}$; for STIS 2011, F(1560Å)=3.5 × 10$^{-14}$ erg cm$^{-2}$ s$^{-1}$ Å$^{-1}$. Note that even though the continuum in 2016 is more than twice as bright as in 2001, the C IV emission line is fainter, particularly in the mid section of the profile. However, the narrow cores of each profile are nearly unchanged. Indeed, in our best fit, the narrow-line component has the same velocity and width, and is within 10% of the flux observed in 2001.

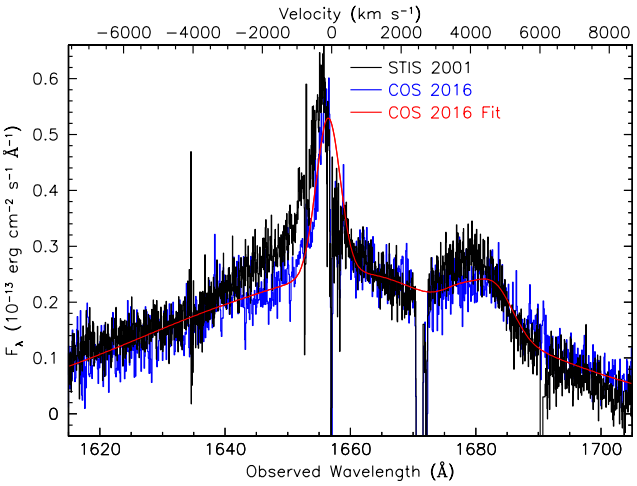


**Fig. 6.** Comparison of STIS and COS spectra of the region surrounding the He II emission line. The black histogram is the average STIS 2001 spectrum. The blue histogram is the unweighted average COS spectrum from the 12 December 2016 and 21 December 2016 observations. Both spectra have the continuum subtracted as well as the underlying emission of the C IV emission line. The STIS spectrum is scaled up by 1.2× to match the flux in the far wings of the COS spectrum. The solid red line is the best-fit emission model for the COS spectrum. The velocity scale along the top axis has zero velocity for He II $\lambda$1640.45 at the host-galaxy redshift of 0.00973 (Theureau et al. 1998). All narrow absorption features are foreground ISM lines.

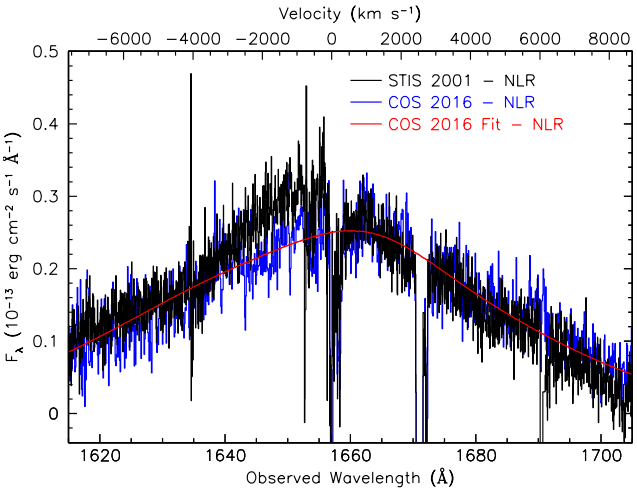


**Fig. 7.** Comparison of STIS and COS spectra of the region surrounding the He II emission line omitting the narrow emission. The black histogram is the average STIS 2001 spectrum with the narrow components of He II and O III] subtracted. The blue histogram is the unweighted average COS spectrum from the 12 December 2016 and 21 December 2016 observations, also with the narrow components subtracted. Both spectra have the continuum subtracted as well as the underlying emission of the C IV emission line. The STIS spectrum is scaled up by 1.2× to match the flux in the far wings of the COS spectrum. The solid red line is the best-fit emission model for the COS spectrum. The velocity scale along the top axis has zero velocity for He II $\lambda$1640.45 at the host-galaxy redshift of 0.00973 (Theureau et al. 1998).

Given the apparently fixed intensity of the narrow-line emission, Figure 9 compares the profiles if we subtract this fitted emission component from the profiles of each spectrum, and from the best fit curve. One can now see that most of the excess emission in the 2001 spectrum is in what we identified as

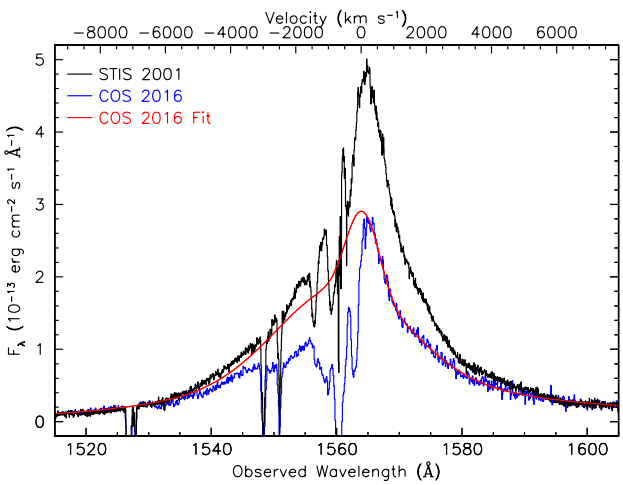


**Fig. 8.** Average STIS spectrum of the C IV region from all observations in the 2000–2001 campaign re-binned into 0.05 Å pixels (black histogram). The blue histogram is the average COS spectrum from 2016. The STIS data have been scaled up by a factor of 1.45 so that the intensities match in the broad wings. The solid red line tracing the data is the total emission model for the average 2016 COS spectrum. The velocity scale along the top axis is for C IV $\lambda$1548.195, relative to the host galaxy systemic redshift, z=0.00973 (Theureau et al. 1998).

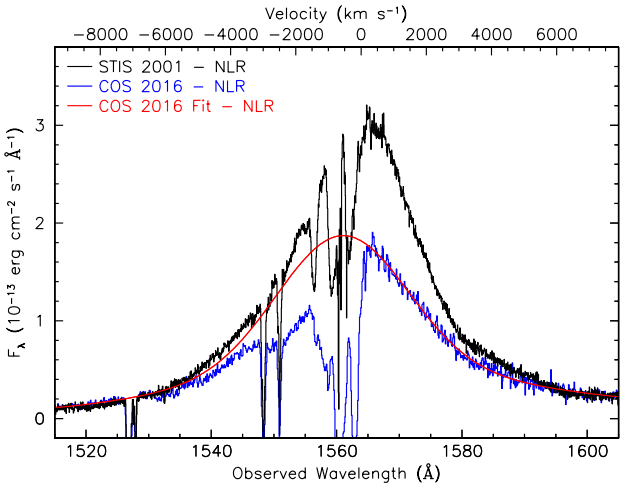


**Fig. 9.** Average STIS spectrum of the C IV region from all observations in the 2000–2001 campaign re-binned into 0.05 Å pixels (black histogram) with the narrow-line component of the fit subtracted from the data. The blue histogram is the average COS spectrum from 2016 with the narrow-line component subtracted. The STIS data have been scaled up by a factor of 1.45 so that the intensities match in the broad wings. The solid red line tracing the data is the total emission model for the average 2016 COS spectrum with the narrow-line component removed. The velocity scale along the top axis is for C IV $\lambda$1548.195, relative to the host galaxy systemic redshift, z=0.00973 (Theureau et al. 1998).

the medium-broad component in Figure 2, which are the blue curves near a systemic velocity of zero in that figure. Note that this component is not needed in our fit to either He II emission profile.

If we now remove this medium-broad component from the STIS spectrum and compare the result to the observed profile in 2016, Figure 10 shows that the shape of the two profiles match well in both the far wings of the line (both red and blue), and on the red side of the line. The minor differences in the profiles on the red side of line center are accommodated by slight

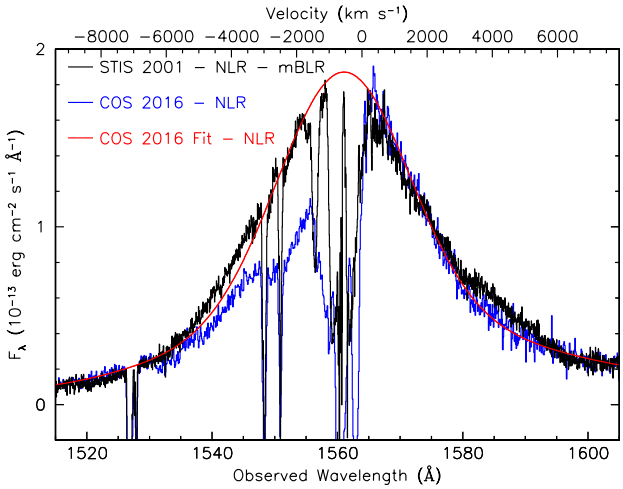


**Fig. 10.** Average STIS spectrum of the C IV region from all observations in the 2000–2001 campaign re-binned into 0.05 Å pixels (black histogram) with both the narrow-line and medium-broad components of the fit subtracted from the data. The blue histogram is the average COS spectrum from 2016 with the narrow-line and medium-broad components subtracted. The STIS data have been scaled up by a factor of 1.45 so that the intensities match in the broad wings. The solid red line tracing the data is the total emission model for the average 2016 COS spectrum with the narrow-line component removed. The velocity scale along the top axis is for C IV $\lambda$1548.195, relative to the host galaxy systemic redshift, z=0.00973 (Theureau et al. 1998).

adjustments in the relative fluxes of the broad and very broad components from 2001 to 2016. However, there is a noticeable deficiency in flux on the blue side of the line profile, which we interpret as absorption due to the appearance of the obscurer.

So, to adapt the C IV profile from 2001 to what we observe in 2016, we fixed the intensity of the narrow-line components at the 2001 value, scaled the intensity of the very broad emission up by the factor of 1.45 required to match the far wings, kept all line centers and widths fixed, and allowed the medium-broad and broad fluxes to vary freely. The result was that the medium-broad component's intensity dropped to nearly zero, with most remaining flux in the broad component. We then freed all parameters (all line centers, widths and intensities) and optimized the fit. Figure 11 shows the best-fit emission model and all its components.

To provide a semi-empirical characterization of the blue-shifted absorption in the C IV profile, we added a series of C IV absorption-line doublets that coincide with the deepest inflection points in the blue wing at outflow velocities of −2590, −4625, −5515, and −6025 km s$^{-1}$. These doublets are modeled as Gaussians in optical depth with relative velocities linked at the ratio of rest wavelengths, identical widths of ∼ 500 km s$^{-1}$ for each doublet component, and blue to red optical depths assumed to have a 2:1 ratio. This characterization enables us in our subsequent modeling to test whether similar absorption is present in other lines such as Ly$\alpha$, N V, and Si IV. The full final model including these additional absorption components is also shown in Figure 11.

Given that there are changes in the C IV profile that do not strictly mimic our comparison of the He II profiles, one might legitimately ask whether the COS 2016 C IV profile could be modeled without invoking absorption components, but allowing for more dramatic changes in the emission-line structure. To test this possibility, we made interactive adjustments to the line centers, widths, and fluxes of the narrow, medium-broad, broad, and very

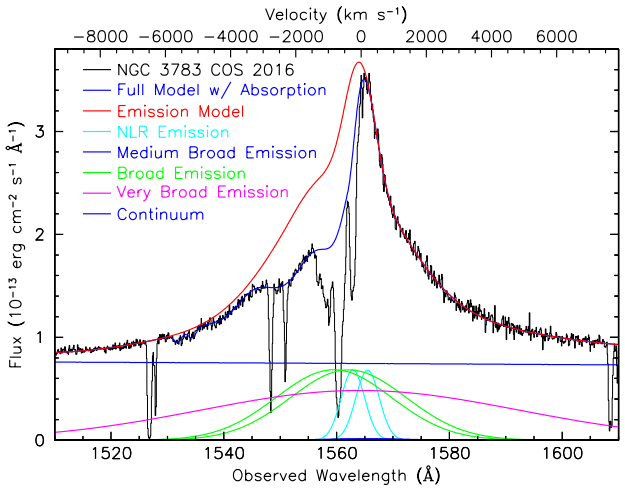


**Fig. 11.** Average COS spectrum of the C IV region from observations in 2016 December (black histogram). The solid red line tracing the data is the total emission model. The solid blue line tracing the data is the emission model modified by components that model the broad absorption. The key in the figure identifies the emission components in our model. The velocity scale along the top axis is for the blue component of the C IV doublet, $\lambda$1548.195, relative to the host galaxy systemic redshift, z=0.00973 (Theureau et al. 1998).

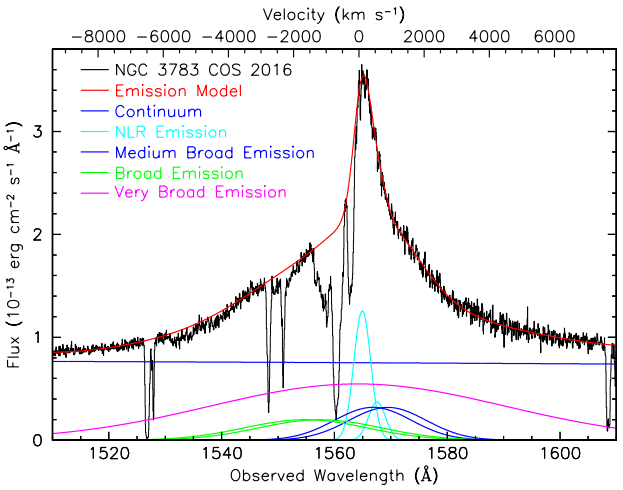


**Fig. 12.** Best fit with no absorption to the average COS spectrum of the C IV region from observations in 2016 December. The data are the black histogram. The solid red line tracing the data is the total emission model. The key in the figure identifies the emission components in our model. The velocity scale along the top axis is for the blue component of the C IV doublet, $\lambda$1548.195, relative to the host galaxy systemic redshift, z=0.00973 (Theureau et al. 1998).

broad components in the C IV profile. We also included the portions of the line profile in the 1530–1545 Å and 1552–1555 Å regions which we had been treating as absorbed and required them to be part of the emission profile. We then let the fit try to optimize itself to the observed profile without including any absorption. Figure 12 shows the resulting fit.

This alternative interpretation of the line profile is not a good fit, and it exhibits several unsatisfactory features. First, there are smaller scale, shallow features on the blue side of the line profile in the −2000 to −6000 km s$^{-1}$ velocity range that are not fit well; these regions still look like shallow absorption features. Second, the narrow emission components have to move in velocity to +100 km s$^{-1}$, and they have an unphysical ratio of 3.4:1 for the blue to red intensity ratio, which should be $\leq$ 2:1. Finally, the medium-broad components have moved in velocity from near systemic in the STIS spectrum to +550 km s$^{-1}$ here, and the broad components have blue-shifted even more to −1650 km s$^{-1}$.

As we noted earlier, the He II profile does not show such dramatic changes. We have tried to correct some of these shortcomings by fixing the narrow emission components in flux and velocity at the STIS 2001 values, forcing the medium-broad components to have zero systemic velocity (as they did in the STIS spectrum), and then let everything else vary freely. As expected, the fit is even worse, and the irregular features on the blue wing of the line profile simply can't be accommodated by such a model. We conclude that absorption is the best explanation for the changes in the shape of the C IV profile.

### 3.2.3. Modeling the Obscured Ly$\alpha$ Profile

To model the Ly$\alpha$ and N V region of the COS spectrum, we start with the emission model developed for the STIS 2001 spectrum. As with C IV, we keep the narrow emission components fixed in flux, velocity, and width. We scale the broader components down in flux to accommodate the decrease in overall flux. Given the convincing evidence for broad, blue-shifted absorption affecting the C IV emission-line profile during the obscured state of NGC 3783, we then impose a scaled replica of the modeled C IV absorption to the the Ly$\alpha$ and N V regions. This initial model for the absorption has the same velocities, widths, and optical depths as for C IV, and provides a very good approximation to the new features present on the red wing of Ly$\alpha$ (that are due to N V absorption) as well as the more subtle changes in the blue wing of Ly$\alpha$. After selecting initial values by eye that give an approximate fit, we then start freeing parameters and iterating to an overall solution as described at the beginning of §3. For our final fit, all parameters vary freely. Figure 13 shows the resulting best fit to the Ly$\alpha$ and N V region. The final model for the Ly$\alpha$ absorption profile resembles the C IV profile closely in velocity and width (see §3.3), but it is shallower in optical depth.

### 3.2.4. Modeling the Obscured Si IV Profile

Modeling the Si IV region is important. Since it is the lowest-ionization species to show significant absorption, it sets a lower bound on the ionization state of the broad absorber. Unlike in NGC 5548 (Arav et al. 2015), absorption from lower ionization species such as Si II or C II are not present in our spectra. Fits to the Si IV region, however, are more ambiguous since the line is not very bright, and the S/N is not as good as in the C IV and Ly$\alpha$ regions. Si IV is also blended with several O IV] transitions; however, these appear to be weak, and as in the STIS spectrum, they primarily affect rest wavelengths > 1403 Å. Starting again with the model for the STIS 2001 spectrum, Figure 14 compares the STIS and COS continuum-subtracted line profiles. No scaling has been applied to either spectrum. Again, we have the remarkable result that despite the continuum being twice as bright in 2016 as in 2001, the emission line in 2001 is slightly brighter. As with C IV, most of this brighter emission is in the core of the line.

As for C IV, we next subtract the narrow emission components of Si IV and O IV]. Figure 15 shows this net spectrum for both epochs. A slight excess still remains near the line center. Recall that we use only 3 Gaussians to model Si IV since it is so weak. This remaining excess present in the STIS spectrum is

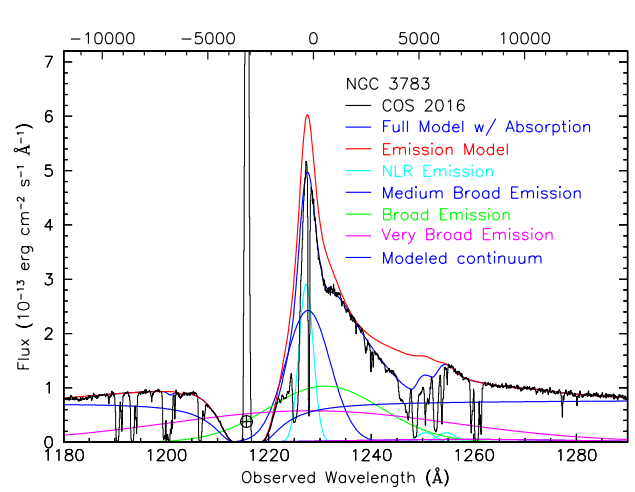


**Fig. 13.** Average COS spectrum of the Ly$\alpha$+N v region from observations in 2016 December (black histogram). The solid red line tracing the data is the total emission model. The solid blue line tracing the data is the emission model modified by components that model the broad absorption. The key in the figure identifies the emission components in our model. Geocoronal emission in the center of the Milky Way Ly$\alpha$ absorption trough is indicated with an Earth symbol. The velocity scale along the top axis is for Ly$\alpha$ $\lambda$1215.67, relative to the host galaxy systemic redshift, z=0.00973 (Theureau et al. 1998).

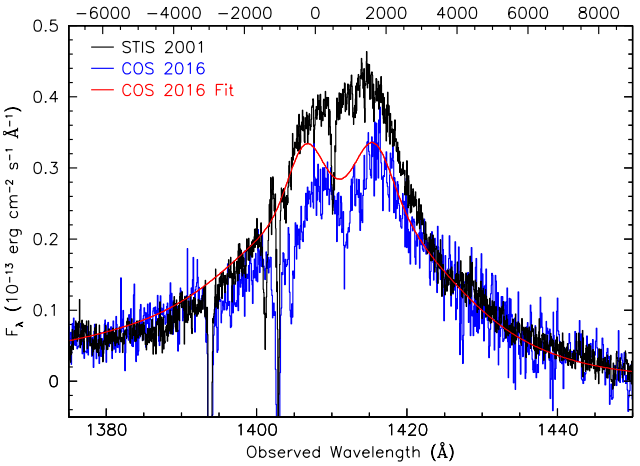


**Fig. 14.** Comparison of STIS and COS spectra surrounding the region of the Si IV emission line. The black histogram is the average STIS 2001 spectrum. The blue histogram is the unweighted average COS spectrum from 2016. The solid red line is the best-fit emission model for the COS spectrum. The velocity scale along the top axis is for Si IV $\lambda$1393.755, relative to the host galaxy systemic redshift, z=0.00973 (Theureau et al. 1998).

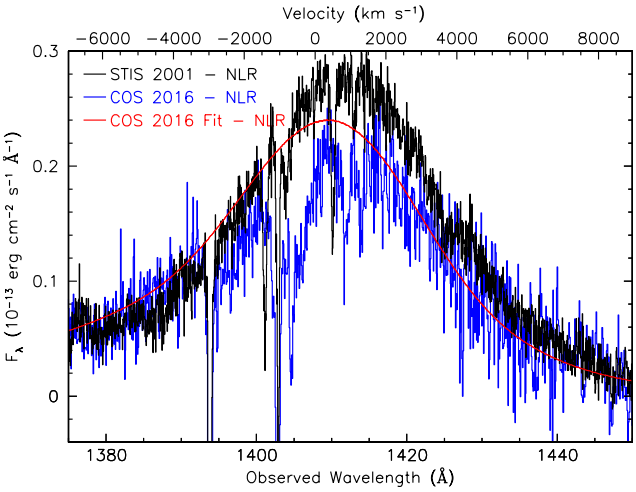


**Fig. 15.** Comparison of STIS and COS spectra of the region surrounding the Si IV emission line omitting the narrow emission components. The black histogram is the average STIS 2001 spectrum with the narrow emission components of Si IV and O IV] subtracted. The blue histogram is the unweighted average COS spectrum from 2016, also with the narrow emission components subtracted. The solid red line is the best-fit emission model for the COS spectrum minus the narrow emission components. The velocity scale along the top axis is for Si IV $\lambda$1393.755, relative to the host galaxy systemic redshift, z=0.00973 (Theureau et al. 1998).

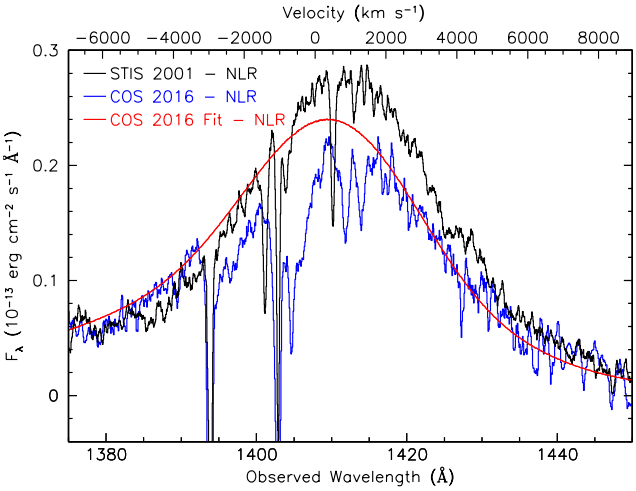


**Fig. 16.** Spectra of the Si IV region as in Figure 15, but with both the STIS and the COS spectra smoothed by a 7-pixel running boxcar filter. The solid red line is the best-fit emission model for the COS spectrum minus the narrow emission components. The velocity scale along the top axis is for Si IV $\lambda$1393.755, relative to the host galaxy systemic redshift, z=0.00973 (Theureau et al. 1998).

analogous to what we have modeled as medium-broad emission in the C IV profile. Removing this would then bring the STIS spectrum almost into line with the model fit to the broad plus very broad emission in the COS 2016 spectrum.

Is there broad absorption present in the COS 2016 spectrum? Near the line peak this is uncertain since the narrow absorption lines are deeper and stronger than in 2001, and they may be responsible for most of the diminution in flux we observe. However, at velocities in the blue wing from −1500 km s$^{-1}$ to −3000 km s$^{-1}$, there is an obvious depression in flux below the model profile. Smoothing both spectra with a 7-pixel running boxcar filter as shown in Figure 16 shows this depression more clearly. The model, however, is far from unique. Given the S/N, an acceptable fit is possible where the only absorption is due to enhanced absorption in the narrow absorption lines. The broad absorption shown in Figures 15 and 16 should therefore be considered upper limits. Relative to the continuum, the depression in flux at −2500 km s$^{-1}$ corresponds to an optical depth of only 0.05.

### 3.2.5. Modeling the Obscured H$\beta$ Profile

Like He II, H$\beta$ emission originates as recombination radiation to an excited level. Similarly, we do not expect absorption in such

**Table 3.** Emission-Line Parameters for the Individual COS 2016 Spectra of NGC 3783

| | | COS 2016-12-12 | | | COS 2016-12-21 | | |
|---|---|---|---|---|---|---|---|
| Feature | $\lambda_0^a$ | Flux[b] | $v_{sys}^c$ | FWHM[d] | Flux[b] | $v_{sys}^c$ | FWHM[d] |
| C III | 1176.01 | 47.0 ± 2.6 | 170 ± 110 | 1490 ± 50 | 34.0 ± 1.5 | 130 ± 20 | 1520 ± 60 |
| Ly$\alpha$ | 1215.67 | 120.0 ± 4.4 | −40 ± 30 | 800 ± 30 | 120.0 ± 4.0 | −40 ± 20 | 800 ± 20 |
| Ly$\alpha$ | 1215.67 | 250.0 ± 8.2 | −240 ± 40 | 4190 ± 40 | 340.0 ± 12.0 | −240 ± 20 | 4190 ± 40 |
| Ly$\alpha$ | 1215.67 | 350.0 ± 11.0 | −70 ± 30 | 6950 ± 20 | 310.0 ± 13.0 | −70 ± 30 | 6950 ± 70 |
| Ly$\alpha$ | 1215.67 | 320.0 ± 9.8 | 60 ± 40 | 18010 ± 70 | 320.0 ± 11.0 | 60 ± 20 | 18010 ± 30 |
| N V blue | 1238.82 | 5.1 ± 0.2 | −40 ± 30 | 980 ± 30 | 7.8 ± 1.2 | −40 ± 30 | 980 ± 50 |
| N V red | 1242.80 | 5.1 ± 0.2 | −40 ± 30 | 980 ± 30 | 7.8 ± 1.2 | −40 ± 30 | 980 ± 50 |
| N V blue | 1238.82 | 7.4 ± 0.3 | −30 ± 30 | 2850 ± 40 | 9.9 ± 0.6 | −30 ± 60 | 2850 ± 20 |
| N V red | 1242.80 | 7.4 ± 0.3 | −30 ± 30 | 2850 ± 40 | 9.9 ± 0.6 | −30 ± 60 | 2850 ± 20 |
| N V | 1240.89 | 25.0 ± 1.0 | −220 ± 170 | 12530 ± 530 | 73.0 ± 2.6 | −220 ± 50 | 12530 ± 40 |
| Si II | 1260.42 | 1.5 ± 0.1 | −150 ± 30 | 1600 ± 40 | 1.7 ± 0.2 | −150 ± 50 | 1600 ± 120 |
| O I+Si II | 1304.46 | 10.0 ± 1.0 | 220 ± 30 | 2500 ± 50 | 11.0 ± 0.4 | 220 ± 40 | 2500 ± 60 |
| C II | 1334.53 | 2.7 ± 0.2 | 110 ± 40 | 2500 ± 20 | 2.8 ± 0.2 | 110 ± 50 | 2500 ± 20 |
| Si IV blue | 1393.76 | 4.6 ± 0.2 | −170 ± 50 | 1110 ± 40 | 4.6 ± 0.2 | −170 ± 30 | 1110 ± 70 |
| Si IV red | 1402.77 | 4.6 ± 0.2 | −170 ± 50 | 1110 ± 20 | 4.6 ± 0.2 | −170 ± 30 | 1110 ± 70 |
| Si IV blue | 1393.76 | 17.0 ± 0.8 | −270 ± 20 | 5140 ± 60 | 28.0 ± 1.2 | −270 ± 30 | 5140 ± 80 |
| Si IV red | 1402.77 | 17.0 ± 0.8 | −270 ± 20 | 5140 ± 60 | 28.0 ± 1.2 | −270 ± 30 | 5140 ± 80 |
| Si IV | 1398.19 | 62.0 ± 2.3 | −2750 ± 30 | 13030 ± 80 | 51.0 ± 1.7 | −2750 ± 40 | 13030 ± 140 |
| O IV] | 1401.16 | 0.7 ± 0.1 | 900 ± 30 | 1110 ± 20 | 0.7 ± 0.1 | 900 ± 40 | 1110 ± 20 |
| O IV] | 1401.16 | 9.1 ± 1.0 | 900 ± 30 | 5140 ± 20 | 9.1 ± 0.4 | 900 ± 40 | 5140 ± 20 |
| N IV] | 1486.50 | 4.1 ± 0.4 | −140 ± 20 | 1110 ± 20 | 2.5 ± 0.3 | −80 ± 20 | 1110 ± 20 |
| N IV] | 1486.50 | 11.0 ± 0.8 | −140 ± 20 | 4330 ± 60 | 6.3 ± 0.9 | −80 ± 20 | 2690 ± 20 |
| C IV blue | 1548.19 | 35.0 ± 1.1 | −60 ± 20 | 940 ± 20 | 38.0 ± 1.9 | −60 ± 20 | 940 ± 30 |
| C IV red | 1550.77 | 35.0 ± 1.1 | −60 ± 20 | 940 ± 20 | 38.0 ± 1.9 | −60 ± 20 | 940 ± 30 |
| C IV blue | 1548.19 | 3.3 ± 0.2 | 140 ± 50 | 2840 ± 20 | 4.8 ± 0.3 | 140 ± 20 | 2840 ± 70 |
| C IV red | 1550.77 | 3.3 ± 0.2 | 140 ± 50 | 2840 ± 20 | 4.8 ± 0.3 | 140 ± 20 | 2840 ± 70 |
| C IV blue | 1548.19 | 190.0 ± 5.7 | −790 ± 20 | 4800 ± 20 | 160.0 ± 5.0 | −570 ± 30 | 4530 ± 30 |
| C IV red | 1550.77 | 190.0 ± 5.7 | −790 ± 20 | 4800 ± 20 | 160.0 ± 5.0 | −570 ± 30 | 4530 ± 30 |
| C IV | 1549.48 | 310.0 ± 11.0 | −220 ± 30 | 13000 ± 120 | 370.0 ± 13.0 | 120 ± 30 | 12500 ± 50 |
| He II | 1640.45 | 14.0 ± 0.7 | 40 ± 20 | 910 ± 30 | 14.0 ± 1.4 | 0 ± 30 | 790 ± 30 |
| He II | 1640.45 | 7.9 ± 0.3 | 2100 ± 100 | 5090 ± 120 | 8.7 ± 0.4 | 1400 ± 110 | 3490 ± 270 |
| He II | 1640.45 | 150.0 ± 4.8 | −120 ± 30 | 11860 ± 60 | 170.0 ± 5.2 | −120 ± 20 | 12530 ± 100 |
| O III] | 1660.81 | 2.3 ± 0.3 | 160 ± 50 | 1220 ± 60 | 3.2 ± 0.1 | 160 ± 30 | 1210 ± 30 |
| O III] | 1666.15 | 4.3 ± 0.5 | 150 ± 20 | 1220 ± 20 | 6.8 ± 0.4 | 160 ± 20 | 1210 ± 20 |
| N III] | 1750.00 | 21.0 ± 0.8 | 0 ± 20 | 3270 ± 30 | 21.0 ± 0.6 | 0 ± 20 | 3270 ± 20 |

**Notes.**

[a] Vacuum rest wavelength of the spectral feature (Å).

[b] Integrated flux in units of $10^{-14}$ erg cm$^{-2}$ s$^{-1}$.

[c] Velocity (in km s$^{-1}$) relative to a systemic redshift of z = 0.00973 (Theureau et al. 1998).

[d] Full-width at half-maximum (km s$^{-1}$).

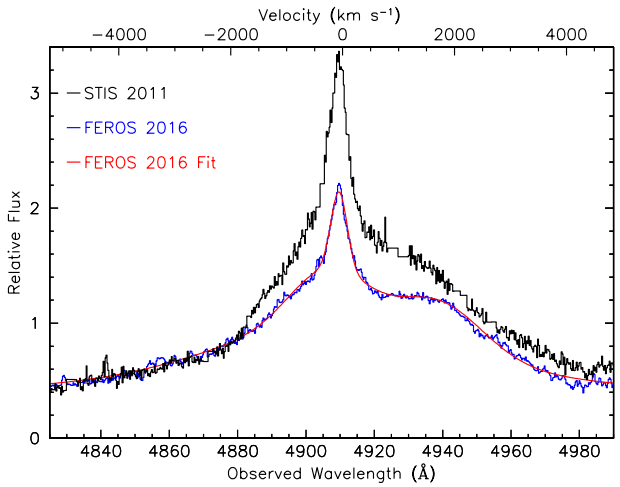


**Fig. 17.** FEROS spectrum of the H$\beta$ region from observations in 2016 December (blue histogram) compared to the STIS spectrum of 2011 (black). The continuum has been subtracted from each spectrum, and the FEROS spectrum has been scaled to match the flux in the far blue wing of the STIS spectrum. The solid red line tracing the FEROS data is the total emission model with the continuum subtracted. The velocity scale along the top axis is for the rest wavelength of H$\beta$ relative to the host galaxy systemic redshift, z=0.00973 (Theureau et al. 1998).

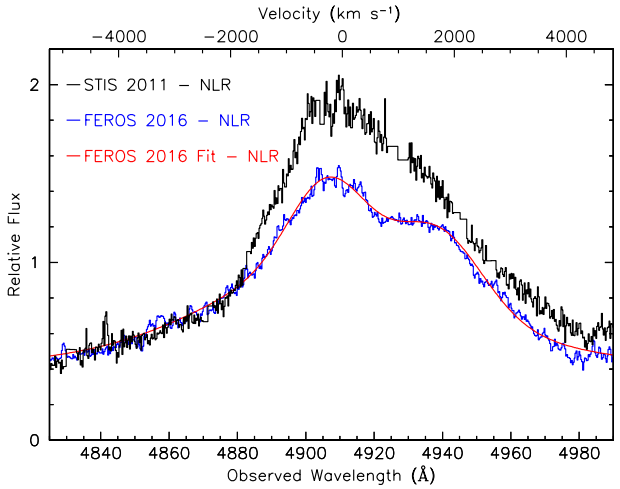


**Fig. 18.** FEROS (blue) and STIS (black) spectra of the H$\beta$ region with the continuum and narrow H$\beta$ emission component subtracted from each. The FEROS spectrum has been scaled to match the STIS spectrum in the far blue wing of the emission line. The solid red line tracing the data is the total emission model with the continuum and narrow emission component subtracted. The velocity scale along the top axis is for the rest wavelength of H$\beta$ relative to the host galaxy systemic redshift, z=0.00973 (Theureau et al. 1998).

a feature. As our baseline for comparison, we use a STIS spectrum obtained in 2011 when NGC 3783 was in an unobscured state. Our FEROS spectrum was obtained on 2016 December 12, simultaneously with our first *XMM-Newton* spectrum of NGC 3783 in its obscured state. Analogous to our fit to the C IV region, we fit both the STIS and the FEROS H$\beta$ spectra using a power law for the continuum, a narrow emission component, a medium-broad component, a broad component, and a very broad component. Significantly, both spectra also require an additional emission bump on the red side of the line profile, although the bump is more prominent in the FEROS spectrum. Figure 17 compares the unobscured STIS spectrum of the H$\beta$ region to the FEROS spectrum. As in our previous comparisons, we have subtracted the continuum and scaled the FEROS spectrum to match the flux level in the far blue wing of the emission-line profile.

In Figure 18, we compare the profiles with both the continuum and the narrow emission component subtracted. The two profiles now show behavior similar to our previous emission-line comparisons–the core of the emission line in the unobscured state is brighter. In the obscured state, this core seems to have faded, analogous to the disappearance of the medium-broad component in C IV. This makes the red emission bump in the H$\beta$ line profile more prominent in the obscured state. These changes can be accommodated simply by changing the relative fluxes of the emission components. There is no need for any absorption in the line profile. All the components in the final best-fit to the FEROS H$\beta$ emission line profile are illustrated in Figure 19.

### 3.3. Photoionization Modeling of the Broad Absorption Lines

Our models of the emission and broad absorption in NGC 3783 now allow us to measure the physical properties of the gas causing the broad absorption and possibly also the soft X-ray obscuration observed in 2016 December. Using our model for the emission spectrum, we produce normalized spectra for the regions affected by the broad UV absorption, as shown in Figure 20.

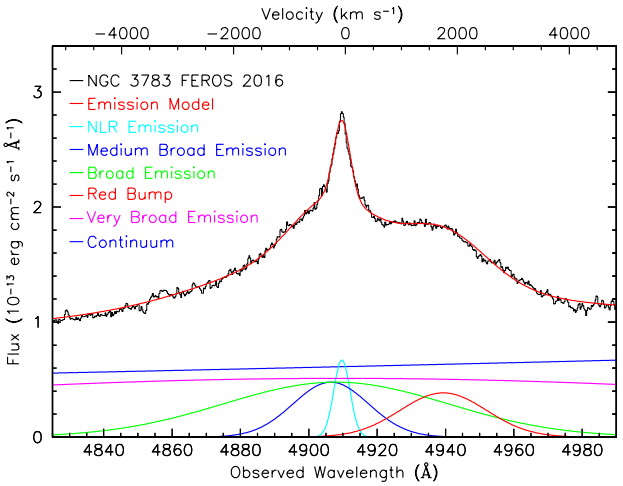


**Fig. 19.** FEROS spectrum of the H$\beta$ region from observations in 2016 December (black histogram). The solid red line tracing the data is the total emission model. The key in the figure identifies the emission components in our model. The velocity scale along the top axis is for the rest wavelength of H$\beta$ relative to the host galaxy systemic redshift, z=0.00973 (Theureau et al. 1998).

We can integrate our normalized models for the broad absorption using the apparent optical depth method of Savage & Sembach (1991) to obtain column densities, $N_{ion}$. However, since the lines appear to be saturated, these column densities are only lower limits to the true column density. In Table 4 we summarize the observable properties of the modeled broad absorption troughs. The equivalent width (EW) is integrated from the normalized spectra between the velocity limits $v_1$ and $v_2$. The deepest point of the trough is at velocity $v_o$, and we use the dispersion $\sigma_v$ to characterize the width of the trough. The covering fraction, $C_f$, is measured by assuming that the profile is saturated at the deepest point of the trough.

Unlike the obscured state of NGC 5548 (Kaastra et al. 2014; Arav et al. 2015), where absorption from low-ionization species

**Table 4.** Properties of the Broad Absorption Troughs in COS Observations of NGC 3783. $\lambda_o$ is the vacuum rest wavelength of the spectral feature. Absorption troughs span the velocity range given by $v_1$ to $v_2$. $v_o$ is the transmission-weighted velocity centroid of the trough, EW is its equivalent width, and log($N_{ion}$) is the inferred ionic column density. Assuming the trough is saturated, $C_f$ is the covering factor at the deepest point in the absorption trough.

| Line | $\lambda_o$ (Å) | $v_1$ (km s$^{-1}$) | $v_2$ (km s$^{-1}$) | $v_o$ (km s$^{-1}$) | $\sigma_v$ (km s$^{-1}$) | EW (Å) | log($N_{ion}$) (cm$^{-2}$) | $C_f$ |
|---|---|---|---|---|---|---|---|---|
| COS 2016-12-12 | | | | | | | | |
| Ly$\alpha$ | 1215.67 | −6960 | 0 | −3000 | 830 | 2.16 ± 0.08 | > 14.58 | 0.18 |
| N v | 1240.51 | −6600 | 0 | −1300 | 1050 | 3.10 ± 0.11 | > 15.66 | 0.37 |
| Si ii | 1260.42 | −6810 | 0 | — | — | < 0.22 | < 13.63 | — |
| C ii | 1334.53 | −6810 | 0 | — | — | < 0.18 | < 14.22 | — |
| Si iv | 1398.27 | −7620 | 0 | −3000 | 2300 | 1.33 ± 0.09 | > 14.48 | 0.08 |
| C iv | 1549.48 | −6810 | 0 | −3000 | 1470 | 6.13 ± 0.21 | > 15.51 | 0.30 |
| COS 2016-12-21 | | | | | | | | |
| Ly$\alpha$ | 1215.67 | −6960 | 0 | −3000 | 860 | 1.25 ± 0.05 | > 14.35 | 0.12 |
| N v | 1240.51 | −6600 | 0 | −1300 | 880 | 2.38 ± 0.09 | > 15.56 | 0.33 |
| Si ii | 1260.42 | −6810 | 0 | — | — | < 0.18 | < 13.68 | — |
| C ii | 1334.53 | −6810 | 0 | — | — | < 0.20 | < 14.13 | — |
| Si iv | 1398.27 | −7620 | 0 | −3000 | 1680 | 1.61 ± 0.10 | > 14.55 | 0.11 |
| C iv | 1549.48 | −6810 | 0 | −3000 | 1320 | 4.05 ± 0.15 | > 15.31 | 0.23 |

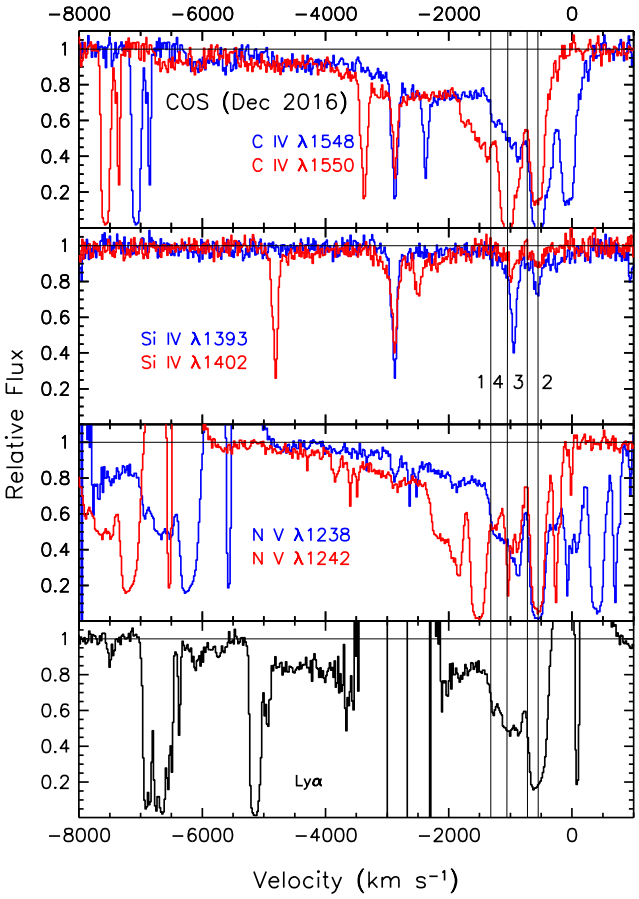


**Fig. 20.** Normalized spectra of the broad absorption features in NGC 3783 (2016-12-12). The velocities of components 1–4 as given by Gabel et al. (2003b) are marked by thin vertical blue lines and labeled.

such as C ii $\lambda$1335 and Si iii $\lambda$1206 was present, in the obscured state of NGC 3783 the lowest ionization broad absorption feature is Si iv. To model the ionization state of the absorbing clouds, we use the unobscured spectral energy distribution (SED) of NGC 3783 as presented in the top panel of Figure 6 of Mehdipour et al. (2017). We derive the ionization balance of the obscurer using a grid of models generated using the Cloudy v17.00 photoionization code (Ferland et al. 2017). Our grid covers a range in ionization parameter log $\xi$ (erg cm s$^{-1}$) from 1.0 to 2.5, and total column density log $N_H$ (cm$^{-2}$) from 21.5 to 23.7. The ionization parameter has the usual definition, $\xi = L_{ion}/(nr^2)$, where $L_{ion}$ is the ionizing luminosity from 1 to 1000 Ryd, $n$ is the density, and $r$ is the distance of the absorbing cloud from the ionization source.

For absorption troughs detected in our spectra, Ly$\alpha$, N v, C iv, and Si iv, we use the lower limits on the total column density given in Table 4 and show these limits as solid lines in Figure 21. Using a transmission profile with the same shape in velocity as C iv, we allow the optical depths at the locations of C ii $\lambda$1335 and Si ii $\lambda$1260 to vary until $\chi^2$ increases by 4.0 above its minimum value. This then gives us $2\sigma$ upper limits (for a single interesting parameter) on their column densities, which are give in Table 4, and shown as dashed lines in Figure 21. (We note that Si iii $\lambda$1206 in NGC 3783 is buried in the damped Ly$\alpha$ Milky Way absorption.) Acceptable photoionization solutions for the broad absorbing gas in NGC 3783 should have ionization parameters and column densities in the region above the solid lines and below the dashed lines. A solid magenta dot in Figure 21 shows the photoionization solution used by Mehdipour et al. (2017) for fitting the X-ray spectrum of NGC 3783. Due to the lack of associated X-ray spectral features, this solution is unconstrained in ionization parameter, but it is tightly constrained in total column density, as shown by the bracketing dashed black lines. Thus the combined UV and X-ray data constrain the photoionization state of the obscuring gas to the small, approximately quadrilateral region surrounding the magenta dot in the figure.

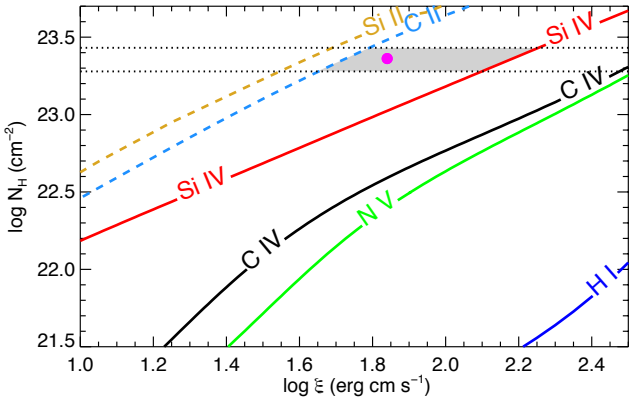


**Fig. 21.** Constraints on photoionization models for the obscurer in NGC 3783. Dotted black lines give the constraints on total column density allowed by our X-ray spectra in Mehdipour et al. (2017). Solid colored lines specify lower limits on the column densities of the indicated ions. Allowed photoionization solutions lie in the space above these lines. Dashed colored lines give upper limits on the column densities of the indicated low-ionization ions. Allowed photoionization solutions lie in the space below these lines. The shaded parallelogram shows the allowed parameter space, and the magenta dot gives the solution used for fitting the X-ray spectra in Mehdipour et al. (2017).

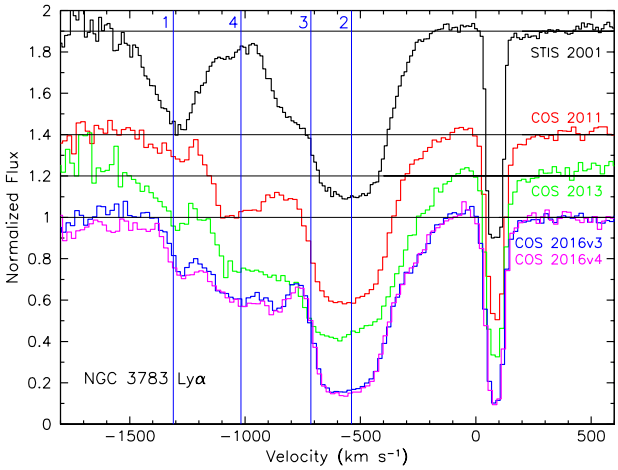


**Fig. 22.** Normalized HST spectra of the Ly$\alpha$ region from five different epochs as labeled. Velocity is for Ly$\alpha$ $\lambda$1215.67 relative to the host galaxy systemic redshift of $z = 0.00973$ (Theureau et al. 1998). Fluxes are normalized to range from 0 to 1. Epochs prior to 2016 are offset vertically by 0.2, 0.4, and 0.9, with the offset normalizations indicated by thin horizontal black lines. The velocities of components 1–4 as given by Gabel et al. (2003b) are marked by thin vertical blue lines and labeled.

### *3.4. Variability of the Narrow Absorption Lines*

The intrinsic narrow absorption lines in NGC 3783 are prominent features in its UV spectrum. The proximity and brightness of NGC 3783 has made it a favorite target for trying to understand the physical characteristics and origin of such intrinsic UV absorption features, and their relationship to the blue-shifted X-ray absorption lines comprising the X-ray warm absorber. The extensive *Chandra*, *HST*, and *FUSE* monitoring campaign in 2000–2001 (Kaspi et al. 2002; Gabel et al. 2003a) established the baseline characteristics of these absorbers. There are four discrete velocity components in the UV. We designate them as #1 through #4 using the nomenclature established by Gabel et al. (2003a). Adjusting the Gabel et al. (2003a) velocities to the zero point of the more precise redshift of Theureau et al. (1998), we will refer to the four components as #1 ($-1311$ km s$^{-1}$), #2 ($-539$ km s$^{-1}$), #3 ($-715$ km s$^{-1}$), and #4 ($-1018$ km s$^{-1}$). Gabel et al. (2005) detected variations in all four components in response to continuum variations as expected for photoionized gas. These variations gave upper limits on the distance of the absorbers in the range 25–50 pc; Component #1 is located more precisely since the density of log n$_e$ = 4.5 cm$^{-3}$ determined using metastable C III* $\lambda$1176 places the absorbing gas at 25 pc. The 15-year baseline of high-resolution *HST* spectra of NGC 3783 enables us to examine the behavior of the intrinsic narrow absorption lines in more detail, and especially in the context of how they have been affected by the obscuration event in 2016.

#### 3.4.1. Kinematics

The variability of the narrow absorption lines in NGC 3783 has been both a boon for our understanding of the UV outflow as well as an enigma. In the extensive 2000–2001 monitoring campaign with STIS, the low-ionization portion of Component #1, designated #1a by Gabel et al. (2005), showed both absorption in the density-sensitive metastable transitions of C III* $\lambda$1176 as well as flux-dependent variability in Si IV that enabled a reliable measurement of the density of the absorbing gas. The puzzling aspect, however, is that Component #1 appeared to change in velocity in the sense that it decelerated over the course of the 2000–2001 campaign (Gabel et al. 2003b). Component #1 appeared to move redward by 90 km s$^{-1}$, from $-1352$ km s$^{-1}$ to $-1256$ km s$^{-1}$. Scott et al. (2014) showed that this motion appeared to continue in their 2013 spectrum, with Component #1 moving near to the apparent location of Component #4 at $-1100$ km s$^{-1}$. They note that there is likely motion in other components as well. Component #3 has disappeared from its original location, and seems to have moved redward into the region originally occupied by Component #2, at least to the blue side of the original trough. However, there is no indication that Component #2 itself has moved redward.

Our new observations in 2016 plus consideration of the intermediate epoch spectrum in 2011 enables us to take a more comprehensive view. In Figures 22, 23, and 24 we show normalized spectra at all four epochs (2001, 2011, 2013, and 2016) for Ly$\alpha$, N V, and C IV. The first thing to notice about the 2016 spectra is that all the absorption features appear to be stronger and deeper. At first this might seem puzzling since the UV continuum in 2016 is brighter than during any of the other epochs. However, this is reminiscent of the behavior of the narrow absorption lines in NGC 5548 during the obscuration event starting in 2014 (Kaastra et al. 2014; Arav et al. 2015; Goad et al. 2016; Mathur et al. 2017; Kriss et al. 2018). Although the visible UV continuum in NGC 3783 is brighter, the soft X-ray obscuration shows that over 70% of the soft X-ray continuum is covered by low-ionization, optically-thick gas. This would imply that only a small percentage of the ionizing continuum is illuminating the narrow absorption-line clouds. In fact, with the obscurer allowing only 26% transmission during the observation on 2016-12-12, the inferred ionizing UV flux is comparable to the faint state during the 2013 observation.

To illuminate these differences in flux more quantitatively, we compare the UV continuum fluxes at wavelengths both longward and shortward of the Lyman limit at 912 Å in Table 5.

**Table 5.** UV Continuum Fluxes in NGC 3783.

| Observation | F(1470Å)[a] | F(912Å)[b] | $T_f^c$ | F(1470Å)[d] (inferred) | F(912Å)[e] (inferred) |
|---|---|---|---|---|---|
| STIS 2001 | 3.76 | 16.4 | 1.00 | 8.47 | 16.4 |
| COS 2011 | 3.52 | 13.3 | 1.00 | 7.98 | 13.3 |
| COS 2013 | 1.53 | 5.9 | 1.00 | 3.51 | 5.9 |
| COS 2016-12-12 | 7.24 | 27.1 | 0.26 | 16.6 | 7.0 |
| COS 2016-12-21 | 7.97 | 30.2 | 0.32 | 18.6 | 9.7 |

**Notes.**
[a] Observed continuum flux at 1470 Å ($10^{-14}$ erg cm$^{-2}$ s$^{-1}$ Å).
[b] Fitted continuum flux extrapolated to 912 Å and corrected for extinction assuming $E(B-V) = 0.107$ ($10^{-14}$ erg cm$^{-2}$ s$^{-1}$ Å).
[c] Fraction of the continuum transmitted by the obscurer (Mehdipour et al. 2017).
[d] Extinction-corrected continuum flux at 1470 Å ($10^{-14}$ erg cm$^{-2}$ s$^{-1}$ Å).
[e] Inferred ionizing continuum flux at 912 Å corrected for extinction and diminished by transmission through the obscurer ($10^{-14}$ erg cm$^{-2}$ s$^{-1}$ Å).

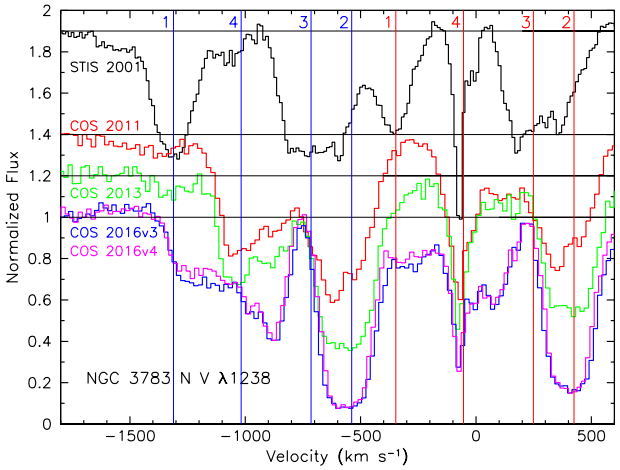


**Fig. 23.** Normalized HST spectra of the N v region from five different epochs as labeled. Velocity is for N v $\lambda$1238.821 relative to the host galaxy systemic redshift of $z = 0.00973$ (Theureau et al. 1998). Fluxes are normalized to range from 0 to 1. Epochs prior to 2016 are offset vertically by 0.2, 0.4, and 0.9, with the offset normalizations indicated by thin horizontal black lines. The velocities of components 1–4 as given by Gabel et al. (2003b) are marked by thin vertical blue lines and labeled; thin vertical red lines mark the expected locations of the red component of the N v doublet.

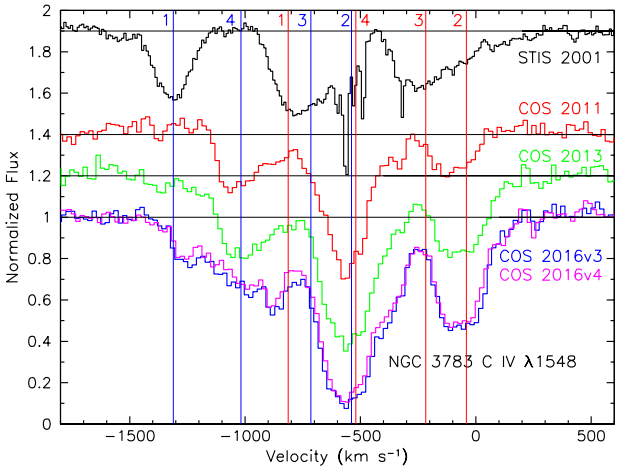


**Fig. 24.** Normalized HST spectra of the C IV region from five different epochs as labeled. Velocity is for C IV $\lambda$1548.195 relative to the host galaxy systemic redshift of $z = 0.00973$ (Theureau et al. 1998). Fluxes are normalized to range from 0 to 1. Epochs prior to 2016 are offset vertically by 0.2, 0.4, and 0.9, with the offset normalizations indicated by thin horizontal black lines. The velocities of components 1–4 as given by Gabel et al. (2003b) are marked by thin vertical blue lines and labeled; thin vertical red lines mark the expected locations of the red component of the C IV doublet.



We start with the observed UV continuum fluxes at 1470 Å for all observations, as measured directly from the spectra. From the models we have fit to each spectrum, we extrapolate the extinction-corrected power law down to the Lyman limit at 912 Å. The column labeled $T_f$ then gives the fraction of light transmitted by the obscurer for each observation, taken from the partial covering models of the X-ray emission in Mehdipour et al. (2017). In the next column we give the extinction-corrected flux at 1470 Å. In the last column, we assume that the fraction of light transmitted by the obscurer is the same as that measured in the soft X-ray, and then calculate the actual flux at 912 Å after it is blocked by the obscurer. Note that no obscurer was present in 2001, 2011, or 2013.

The consequences of the obscuration in NGC 3783 are most apparent in low-ionization lines such as Si IV (Fig. 25) and C III* $\lambda$1176 (Fig. 26). Figure 25 compares spectra of the Si IV region at all epochs in calibrated flux units. During the 2001 campaign, Si IV absorption appeared only in Component #1, most prominently during low-flux states (Gabel et al. 2005). Note that there is no Component #4 absorption in Si IV during 2001; in fact, it is only noticeable as a strong feature in O VI in the *FUSE* spectrum (Gabel et al. 2003b). Component #1 shifted in velocity gradually redward during the 2000–2001 campaign (Gabel et al. 2003b), and Scott et al. (2014) suggest that the absorption appearing near the velocity of Component #4 in 2013 is actually the continued redward evolution in velocity of Component #1. In the low-flux state of 2013, having "moved" to the location of Component #4, it appears again. Similarly, Si IV absorption in Component #2 only appears in low-flux states. Likewise, C III* $\lambda$1176 absorption was only associated with Component #1 in the 2000–2001 campaign, and was strongest in the low states (Gabel et al. 2005).

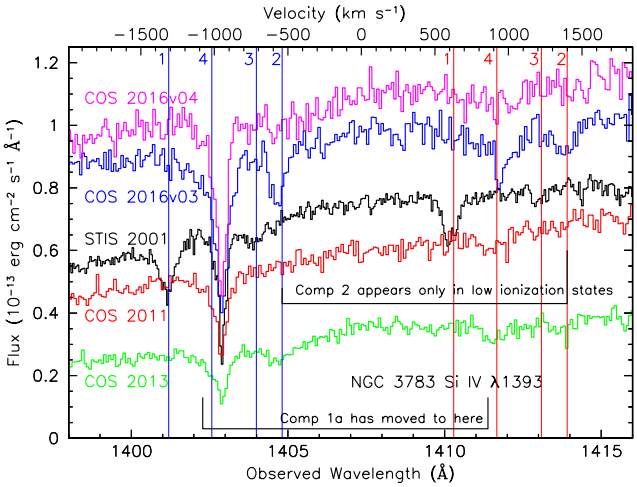


**Fig. 25.** HST spectra of the Si IV region from five different epochs as labeled. Fluxes and wavelengths are as observed. The wavelengths of components 1–4 as given by Gabel et al. (2003b) are marked by thin vertical blue lines and labeled; thin vertical red lines mark the expected locations of the red component of the Si IV doublet. Note that absorption in Component #2, which is strong only in low-flux states in all prior observations, appears strongest during the 2016-12-12 COS observation, which was taken at the time that X-ray obscuration was strongest. Also, the low-ionization Component #1a, which is the "decelerating" absorption-line cloud (Gabel et al. 2003b; Scott et al. 2014), has decelerated to an observed wavelength of 1403 Å, where it is blended with Galactic Si IV $\lambda$1403.

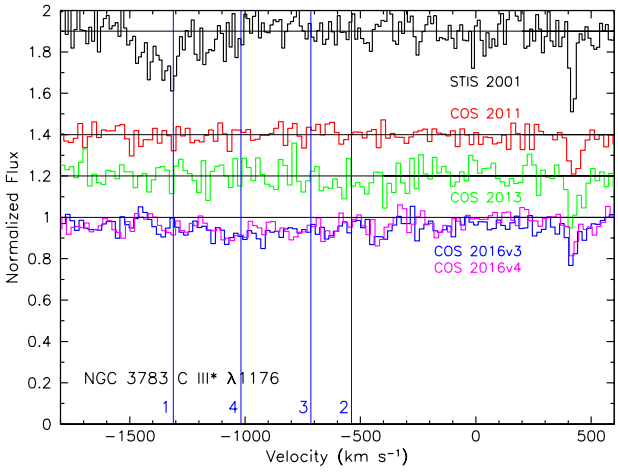


**Fig. 26.** Normalized HST spectra of the C III* $\lambda$1176 region from five different epochs as labeled. Velocity is for the strongest C III* $J = 2$ transition at 1175.71 Å relative to the host galaxy systemic redshift of $z = 0.00973$ (Theureau et al. 1998). Fluxes are normalized to range from 0 to 1. Epochs prior to 2016 are offset vertically by 0.2, 0.4, and 0.9, with the offset normalizations indicated by thin horizontal black lines. The velocities of components 1–4 as given by Gabel et al. (2003a) are marked by thin vertical blue lines and labeled.

As Fig. 26 shows, C III* $\lambda$1176 has reappeared during the 2016 obscuration observations as a shallow depression near the original velocity of Component #4, but more likely representing the evolution in velocity of gas associated with Component #1. As Table 5 shows, the ionizing flux at 912 Å in 2016 is nearly as low as in 2013, if most of the intrinsic continuum is hidden by the obscurer. This shadowing of the narrow-absorption-line gas by the obscurer then explains the appearance of absorption associated with Components #1 and #2 during the obscuration event in 2016.

### 3.4.2. Photoionization Response

Several factors complicate the interpretation of the absorption-line profiles in NGC 3783. As Gabel et al. (2003a) showed in their analysis of the full Lyman series using both the STIS and FUSE spectra, Ly$\alpha$ is heavily saturated. The absorption lines are broad and blended. In C IV, the velocity spacings lead to overlap between the blue and red lines of the C IV doublet for Components #1 and #3, and for #2 and #4. In N V the individual troughs are only slightly blended, but the red transition of Component #4 is contaminated by foreground interstellar absorption by S II $\lambda$1250. Since N V has the cleanest profiles, we use it as a starting point for all of our analysis. In the three-year interval from 2013 to 2016, note that the figures show little additional apparent motion of Component #1. In fact, its motion appears to have halted by the time of the 2011 spectrum, where its location differs little from 2013 or 2016. Another intriguing aspect of our 2016 spectra is that absorption near the original position of Component #1 has re-appeared.

Absorption at the original locations of Components #2 and #4 show a clear ionization response, perhaps indicating that these are stable, persistent features. Absorption at the velocity of Component #4 only appears in the low flux state of the COS 2013 observation. Initially it may seem surprising that it is also present in the first observation on 2016-12-12 (and not strongly in the second), but this can be understood as another example of the line-of-sight shadowing by the transient soft-X-ray obscuration, as for the NGC 5548 obscurer (Arav et al. 2015). If the UV flux is scaled down by the transmission of the obscurer (only 26% for the 2016-12-12 observation), the inferred ionizing flux is actually *lower* than in 2013. Similarly, in the 2016-12-21 observation, the obscuration is not as opaque, the intrinsic continuum is slightly brighter, and the inferred ionizing flux is *higher* than for the COS 2013 observation.

Similar arguments apply to the depth of the red side of the absorption trough in Component #2, although the interpretation is slightly more complicated due to the different covering fractions of the line and continuum for this feature, and the strongly varying intensity of the emission lines relative to the continuum among the HST observations of NGC 3783. Based on the analysis of the Lyman lines, Gabel et al. (2003a) show that the narrow absorption features have different covering factors for the lines and the continuum. The depth of the troughs in Ly$\alpha$, which is certainly saturated, for the 2016 observation show that over 92% of both line and continuum is covered.

To try to unravel the behavior of the narrow absorption components, we also have examined their changing structure in the context of potential responses to changes in the ionizing flux illuminating the absorbing clouds or filaments. We start with the structures at the highest blue-shifted velocities, Component #1, then Component #4, #3, and #2.

**Component #1.** This component was strong and well defined in 2001 (and earlier). As described by Gabel et al. (2005), it appears to have both a low-ionization component, #1a, that appears in all ionic species, including Si IV and C III*. It is blended with a high-ionization portion called 1b, which is needed to explain the N V and O VI strengths. It is the low-ionization portion, #1a, that appears to decelerate (Gabel et al. 2003b), although the shift in the line centroid is seen in all ions. The most definitive detection is in our 2016-12-12 observation (v3), where it

appears in both Si IV and C III*. The C III* absorption associated with Component #1 in 2016 appears as a broad, shallow depression at the velocity of Component #4, visible in Fig. 26.

Similarly, the Ly$\alpha$ absorption formerly associated with Component #1 in 2001 has also shifted to the position of Component #4 in the 2011, 2013, and 2016 spectra. This new location for #1a also shows an apparent response to ionizing flux in that it is deepest for the 2013 spectrum, followed by 2016, and then 2011. This is consistent with higher neutral hydrogen column densities during observations with lower *ionizing* flux (i.e., observed UV flux corrected by transmission of the obscurer).

This apparent motion in Component #1a seems to have separated it kinematically from the high-ionization Component #1b. Just redward of the 2001 velocity of Component #1, a new component appears in 2011 in Ly$\alpha$ at $-1280$ km s$^{-1}$. We suggest that this is the counterpart to high-ionization Component #1b. It also shows an apparent response to changes in the ionizing flux, being deepest in 2013 and 2016, and shallower in 2011. Note that this velocity is also more consistent with the blue side of the X-ray absorption troughs in the high ionization ions, e.g., Figure 9 of Scott et al. (2014), comparing profiles for Mg XI and Mg XII to the UV ion N V.

The behavior of this feature in N V and C IV corroborates its identification as the high-ionization Component #1b. The feature stands out as well defined in N V and C IV in spectra from 2016 when the ionizing continuum was obscured, but appears only weakly in the prior spectra. As shown by the photoionization models in Figure 7 of Gabel et al. (2005), this is consistent with it having an ionization parameter log U > $-1.5$ (log $\xi > 0.0$), lying well beyond peak ionization for N V and C IV during 2001 and 2011, but accumulating higher column densities in those ions at the lower ionization parameters more likely present during the obscured state.

**Component #4.** As noted by Scott et al. (2014), the original Component #1 appears to have moved to the velocity of Component #4. In N V this transition in velocity happened by the time of the 2011 observation. There is no discernible change in velocity between 2011 and 2013, but the feature is much weaker in 2016.

In addition to this possible motion of Component #1a, another trough appeared redward of the Component #4 location at $-880$ km s$^{-1}$ in 2011, and this feature persists in 2013 and 2016. Its depth has no relation to the strength of the ionizing flux–it is weakest in 2013 when the ionizing flux was weakest, stronger during the bright 2011 epoch, and at its strongest during the 2016 obscuration event. However, in Ly$\alpha$ this feature shows a more consistent response to changes in the ionizing flux level. It is strongest in 2013 when the ionizing flux level was lowest, weakest in 2011 when it was highest, and in between during the epoch of obscuration in 2016.

**Component #3.** Component #3 essentially disappears after 2001. Scott et al. (2014) note its absence in 2013, but it is also not present in the 2011 or the 2016 spectra.

**Component #2.** Component #2 was the most prominent absorber in Ly$\alpha$ in 2001, but it was not exceptionally strong in any other ion. Starting in 2011, it develops a profile in N V and C IV more similar to its appearance in Ly$\alpha$. Variations in Component #2 are analyzed most cleanly in the N V transitions, where it is unblended. It is saturated at all epochs in Ly$\alpha$, and it is only visible in low-ionization epochs in Si IV (2013 and 2016). In C IV, the blue component overlaps the red trough of Component #4, or the "decelerated" red trough of Component #1a. The red trough of Component #2 is unblended. It therefore can be used to corroborate inferences derived from analysis of the N V doublet, but it cannot provide an independent measure of covering fraction and optical depth.

The transition in the morphology of the Component #2 absorption profile from 2001 to 2011 is suggestive of (1) Component #3 having decelerated from its position in 2001 to form the blue side of the Component #2 trough, and (2) the red half of the trough corresponding to the original 2001 location of Component #2. The evolution in strength of Component #2 is consistent with a response to changes in the ionizing flux. In 2001, when the ionizing UV flux was strongest, Component #2 was at its weakest. During the obscured epoch of 2016, when the ionizing UV is weakest, Component #2 has its deepest troughs, with the N V profile having an appearance similar to the saturated Ly$\alpha$ profile. The intermediate depths in 2011 and 2013 are in proportion to the relative strengths of the UV flux at those epochs, both of which were fainter than 2001. The red transition of Component #2 in C IV shows this same pattern of changes in trough depth. Since Ly$\alpha$ is strongly saturated, this suggests that this component is highly ionized, as shown in Figure 7 of Gabel et al. (2005), with the C IV and N V ionization fractions being well past their peaks.

## 4. Discussion

Our simultaneous UV spectra of NGC 3783 quantify the broad, fast absorption that appeared in the blue wings of the high-ionization UV resonance lines at the same time as the appearance of strong soft X-ray obscuration (Mehdipour et al. 2017). Our detailed analysis of the emission-line profiles show that broad absorption on the blue wings of the permitted emission lines (and the absence of absorption in excited-state lines such as He II$\lambda$1640 and H$\beta$) provides a more physically consistent description than an arbitrary set of emission components. Combining the spectral diagnostics of the obscurer in our UV observations with the total column density measured with the X-ray spectra enables us to determine the ionization state (log $\xi = 1.84^{+0.4}_{-0.2}$ erg cm s$^{-1}$) and kinematics of the outflowing gas responsible for the obscuration. Indeed, without the UV observations, it would not even have been possible to assert that the soft X-ray obscuration was due to an outflow since there are no prominent spectral features in the heavily absorbed X-ray spectrum. Our UV spectra show that the absorption extends from near zero velocity to a maximum of $\sim -6200$ km s$^{-1}$, with a flux-weighted mean of $-2840$ km s$^{-1}$.

As in NGC 5548 (Kaastra et al. 2014), the strength and depth of the UV absorption varies in concert with variations in the X-ray obscuration. When the obscuration is strongest, on 12-Dec-2016, the UV absorption is strongest. As the obscuration lessened, as shown in the 21-Dec-2016 observation with *XMM-Newton*, the UV absorption also diminished. This could be seen not only in the depths of the broad absorption features, but also in its inferred influence on the ionizing UV continuum. Low-ionization features in the intrinsic narrow absorption lines of NGC 3783 such as C III* $\lambda$1176 and Si IV $\lambda\lambda$1393,1402 become deeper when the X-ray obscuration is strongest. As in NGC 5548 (Arav et al. 2015), this argues that the X-ray/UV obscurer lies interior to the clouds producing the intrinsic narrow absorption lines.

Nearly two decades of high spectral resolution observations of the narrow absorption-line features in NGC 3783 show that they are not as kinematically stable as other AGN we have studied intensively, for example, Mrk 509 (Kriss et al. 2011; Arav et al. 2012), or NGC 5548 (Arav et al. 2015). The variations in the narrow absorption lines in NGC 3783 discussed in §3.4

**Table 6.** C IV Emission-line Fluxes and Equivalent Widths in NGC 3783.

| Observation | F(1470Å)[a] | C IV Flux[b] | C IV EW[c] |
|---|---|---|---|
| STIS 2001 | 3.76 | 718 | 204 |
| COS 2011 | 3.52 | 676 | 200 |
| COS 2013 | 1.53 | 504 | 343 |
| COS 2016 (average) | 7.67 | 777 | 104 |

**Notes.**
[a] Observed continuum flux at 1470 Å ($10^{-14}$ erg cm$^{-2}$ s$^{-1}$ Å).
[b] Total observed C IV emission-line flux (($10^{-14}$ erg cm$^{-2}$ s$^{-1}$).
[c] C IV emission-line equivalent width (EW) (Å).

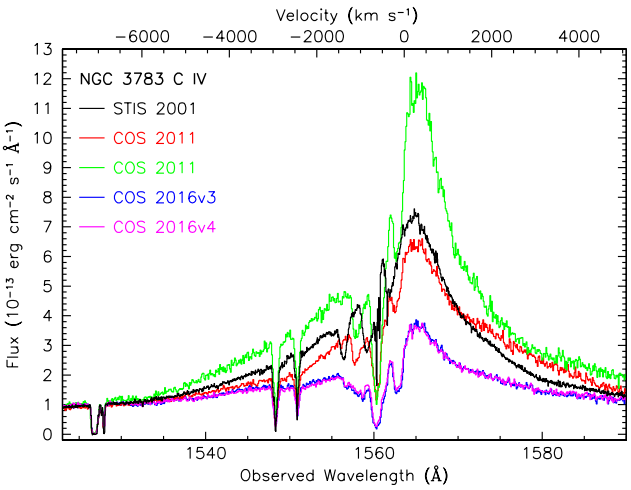


**Fig. 27.** Comparison of the C IV emission line profiles for NGC 3783 in the observations with STIS 2001 (black), COS 2011 (red), COS 2013 (green), and COS 2016 Visit 3 (blue) and COS 2016 Visit 4 (magenta). The profiles have all been scaled to the flux level of COS 2016 Visit 4 at 1525 Å.

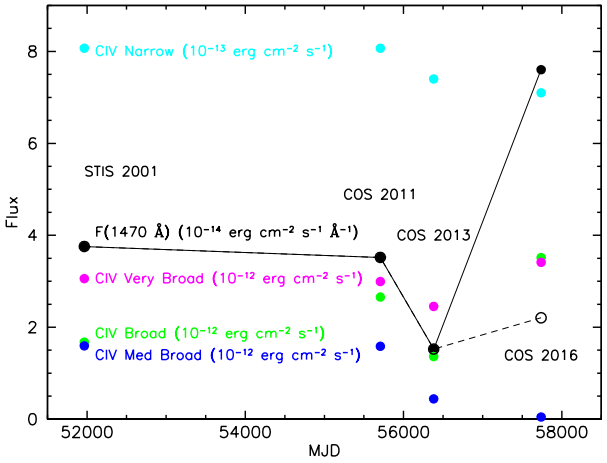


**Fig. 28.** Fluxes at the epochs of the STIS 2001, COS 2011, COS 2013, and COS 2016 observations of NGC 3783 in the continuum at 1470 Å (black) and in the several components of the C IV emission line: the narrow component (cyan), the medium-broad component (green), the broad component (blue), and the very broad component (magenta). Fluxes are scaled as noted in the labels in the figure. The continuum points are connected by a thin black line. The open circle in 2016 shows the value of the continuum flux if we scale it down by the transmission of the obscurer at the epoch of the COS observations.

show that the behavior of these absorption features is not as simple as the stable absorption troughs seen in NGC 5548. In NGC 5548, these troughs maintain their velocities; they show variations consistent with constant column density and covering factor and simple changes in ionic column density determined purely by variations in the ionizing flux. In NGC 3783, even for features that seem to have been stable in velocity from 2011 to 2016, we see changes in both ionic column density and in covering factor. Although some column-density changes are correlated with changes in ionizing flux (e.g., Component #1a and Component #2), others are not (Component #1b, Component #3, and Component #4). Thus, we must be viewing configurations of absorbing clouds that are clumpy, and possibly changing their arrangement along the line of sight. Given the relative stability in velocity of some of the features, it seems that rather than having clouds or filaments crossing our line of sight, or decelerating, that an alternative possibility might be that the multiple velocities we see are associated with dense clouds or filaments that are moving at fixed velocity. These dense entities are a source of material, and, in and of themselves, they have low enough covering fraction so as not to cause noticeable absorption. The absorption we see is then caused by material ablated or evaporated from the outer portions of these dense sources. This material is photoionized, heats up, expands, and thus varies in covering fraction and ionization, giving rise to the variable features we see. Dense knots like this that form and evaporate can form naturally as thermal instabilities in a radiatively accelerated flow (Proga & Waters 2015).

Rather than invoking deceleration to explain the changing kinematics of these clumps, transverse motions of clouds along our line of sight seems more plausible. These transverse motions may be related to velocity shear in outflowing streamlines that have both radial and toroidal motions defining their outflow trajectories. Based on the measured electron density and column density of Component #1b, Gabel et al. (2005) infer a transverse size of $10^{16}$ cm for a uniform cloud. At the distance of 30 pc based on the photoionization solution, Keplerian velocities at this location would be of order 200 km s$^{-1}$, which would include the gravitational potential of the host galaxy as well as the black hole. Thus it would take 2.1 years for the cloud to traverse our line of sight. Since we see dramatic changes in 10 years or less, if these were caused by transverse motion, the cloud would have to be elongated along our line of sight by a factor of 10 relative to its width. If “clouds" are really filaments, perhaps organized along streamlines or magnetic field lines (e.g., Fukumura et al. (2010)), this is not implausible.

### 4.1. Structure and Evolution of the Broad Line Region

Based on the X-ray partial covering of the obscurer, which suggests its transverse size is comparable to the size of the X-ray emitting continuum region, and the variability timescale of ∼ 1 day in the X-ray, Mehdipour et al. (2017) infer a density of ∼ $2.6 \times 10^9$ cm$^{-3}$ and an approximate location of ∼ 10 lt-days from the source. The location, density, and the kinematics of the obscuring outflow all suggest that it may be associated with the broad line region in NGC 3783. As we showed in §3, the broad emission line profiles have also changed substantially between 2001 and 2016.

The extensive reverberation mapping campaign conducted on NGC 3783 in 1992 by the International AGN Watch (Re-

ichert et al. 1994; Stirpe et al. 1994; Onken & Peterson 2002) showed that the UV emission lines respond to variations in the continuum flux as expected if they are reprocessing the ionizing radiation from the central source. Refined analysis of these data (Onken & Peterson 2002) determined a mean lag for the C IV emission line of 3.8 days. During the 1992 campaign, the line fluxes tracked the continuum closely, with no dramatic changes in the line profile. However, as demonstrated in §3, the broad emission line profiles observed by COS in 2016 differ dramatically from those seen with STIS in 2001. The archival COS observations from 2011 and 2013 enables us to study the evolution of these profiles. We have fit both of these spectra using the same procedures as for the unobscured STIS spectrum. The best-fit parameters for each are tabulated in Table 7. To show a more comprehensive history of these variations, we compare the C IV emission line profiles for all four epochs from 2001 to 2016 in Figure 27. The most striking aspect of this comparison is the large variation in equivalent width among these observations. Table 6 summarizes the total fluxes and equivalent widths (EW) of the C IV emission lines at all four epochs in our study. Note that although both the continuum and the C IV flux were at a maximum in 2016, the equivalent width was at a minimum. Conversely, when flux was at a minimum in 2013, the equivalent width was at a maximum. The narrow core of the line dominates the emission profile (at velocities $< 500$ km s$^{-1}$) in 2013, but it makes only a minor contribution in 2016. In fact, the narrow component stays relatively constant in flux, similar to the narrow core in NGC 5548 (Crenshaw et al. 2009).

Figure 28 shows these variations quantitatively. The very broad component varies roughly in proportion to the variations in the continuum flux. The medium-broad (FWHM~2838 km s$^{-1}$) component shows the most variation, virtually disappearing during the COS observations of 2016. This same kinematic component is also much weaker in the N V, Si IV, He II, and H$\beta$ line profiles.[3] Although our decomposition of the line profile is not unique, given the kinematic relationships between line width and reverberation lags established in many reverberation campaigns, we can roughly decompose the C IV emission-line profile into a correspondence between width and distance from the central source using the corresponding Keplerian orbital velocities in the potential of the $2.35 \times 10^7$ M$_\odot$ black hole (Bentz & Katz 2015) in NGC 3783. The Keplerian velocity corresponding to the mean lag of 3.8 lt-days is 5630 km s$^{-1}$. For our model of the C IV profile, the narrow core (937 km s$^{-1}$) lies at a distance of 137 lt-days, the medium-broad component (2838 km s$^{-1}$) at 15 lt-days, the broad component (4576 km s$^{-1}$) at 5.8 lt-days, and the very broad component (10030 km s$^{-1}$) at 1.2 lt-days.

In the context of our model of the line profile, both 2013 and 2016 represent unusual states for the broad line region of NGC 3783. Overall, the continuum in 2013 is 2.5–5x fainter than in 2001 or 2016, yet the very broad component of the C IV emission-line flux is dimmer by only 20–30%. If the BLR is reprocessing continuum radiation, to compensate for the reduced continuum flux and still radiate nearly as profusely, the covering factor of the very broad portion of the C IV profile must be higher. This implies that in the faint state of 2013, the inner part of the BLR must have puffed up vertically. At the same time, we note that the medium-broad component at 2838 km s$^{-1}$ virtually disappeared in 2016.

[3] The medium-broad component of Ly$\alpha$ does not share this behavior. Strong absorption due to damped Milky Way Ly$\alpha$ absorption blends with all components on the blue wing of Ly$\alpha$ in NGC 3783 and adds considerable degeneracy to our decomposition of the line profile.

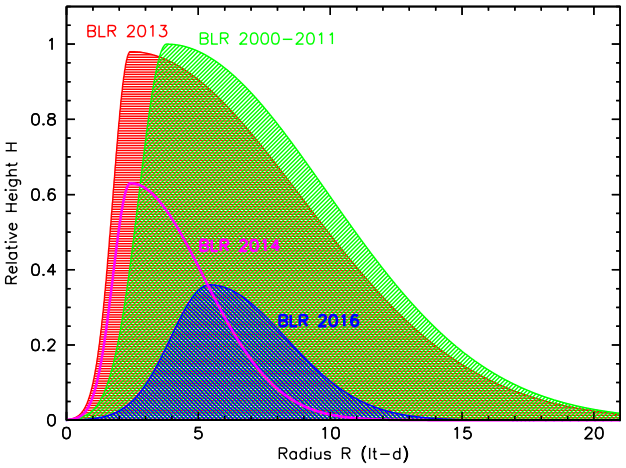


**Fig. 29.** Schematic representation of the evolution of the BLR in NGC 3783 The green shaded area represents the vertical structure and radial extent of the BLR during the period from 2000 to 2011. The red shaded area shows the inferred structure in 2013, when the continuum flux was 2.5x less, but the EW of C IV was 70% higher. The magenta curve is the hypothetical structure in 2014, when the continuum flux was still low after the BLR had dynamically adjusted to the lower flux level. The blue shaded area is the inferred structure at the time of the obscuration event in 2016.

We can interpret these changes in the context of recent models in which a dust- and line-driven wind from the accretion disk create the BLR (Czerny & Hryniewicz 2011; Czerny et al. 2017; Baskin & Laor 2018). Although these models do not yet quantitatively predict sizes and velocities for the BLR that match the emission-line profiles and velocities observed in typical AGN (Czerny et al. 2017), they offer a physical framework that may explain some of the qualitative changes we observed in the spectra of NGC 3783 over the years. We hypothesize that the dramatic drop in continuum flux in 2013 (or shortly before) initiated a reconfiguration of the BLR in NGC 3783. Figure 29 illustrates this evolution schematically.

From the 1992 reverberation-mapping campaign through the STIS observations in 2000–2001 and the COS observation in 2011, the broad-line profiles in NGC 3783 remained similar in shape and equivalent width. This apparently stable configuration is represented in Figure 29 by the shaded green area. The shape is chosen to resemble line emissivity distributions typical of reconstructions from reverberation-mapping results (Krolik et al. 1991; Grier et al. 2013). The peak is set at the C IV mean lag of 3.8 lt-days. To scale this configuration to other epochs in the history of NGC 3783 observations, we use the scaling relations of Baskin & Laor (2018) for a dusty wind-driven BLR. The peak radius of the broad line region, $R_{BLR}$, scales with luminosity, L, as $R_{BLR} \sim L^{1/2}$. The height of the broad line region, H, also scales with luminosity as $H \sim L^{1/2}$. Thus, when the continuum brightness drops in 2013, the peak of the BLR emissivity shifts to a lower radius, R=2.4 lt-days. Of course, the BLR can not change its shape instantaneously. For the radiation-pressure driven winds in the Czerny et al. (2017) and Baskin & Laor (2018) models, the relevant timescale is the local dynamical timescale for material moving up or down from the accretion disk, set by the vertical component of the gravitational force exerted by the central black hole. The free-fall time for material

falling back to the disk after the radiation pressure disappears is

$$t_{ff} = \left(\frac{2R^3}{GM_{BH}}\right)^{1/2}.$$

So, in 2013, the location of peak emissivity is expected to move inward to 2.4 lt-days in response to the reduced brightness of the central source and the accretion disk. The expected BLR height at that location would also be expected to be lower, at ∼ 64% of the peak height in 2000-2011. However, it is likely that highly ionized gas above the disk would drop in ionization very quickly, producing BLR-like emissivity at large heights. The red shaded area in Figure 29 reflects the smaller $R_{BLR}$, but a height consistent with the higher observed equivalent width of the C IV emission line. Gas at these heights either at small radii in the disk or at larger radii can not be supported via radiation pressure, but the dynamical adjustments in the vertical extent of the BLR would take months to years to adjust to this lower luminosity. At 2.4 lt-days, the timescale is $t_{ff}$ = 0.3 years; at 10 lt-days, the peak radius for H$\beta$ in the 1992 reverberation campaign, it is 3.4 years. The red shaded area in Figure 29 reflects these delays. We do not know when the drop in continuum flux actually occurred prior to the 2013 COS observation, but the large equivalent width observed in the emission lines implies that gas at those innermost radii has not yet had time to fall back toward the disk. Therefore we infer that the drop in flux happened very soon before the 2013 observation. Similarly, since the gas at larger radii would take years to fall back, the red shaded area shows a similar height to the prior shape represented by the green shaded area.

We have no observations of NGC 3783 in 2014, so the magenta curve in Figure 29 is a hypothetical view of how the BLR would have responded dynamically to the lower flux observed in 2013, had it remained at that low flux level. By then, gas at heights supported by the normal flux state in 2000–2011 would have had time to fall back toward the accretion disk. The peak height of the BLR is adjusted by the square root of the flux ratios between 2001 and 2013, and the vertical extent of the BLR at all radii drops significantly due to the loss of radiation-pressure support.

*Swift* observations of NGC 3783 (Kaastra et al. 2018) show that NGC 3783 was still in a low flux state in mid-to-late 2016, several months before the obscuration event in late 2016 (Mehdipour et al. 2017). Therefore, even though NGC 3783 had brightened dramatically, gas in the BLR would not have had time to move in response to these changes. The blue shaded area in Figure 29 shows the peak of the BLR emissivity moving to a larger radius, 5.4 lt-days, but not changing much in vertical height since it has not yet had time to respond dynamically to the increased radiation pressure. The height shown in Figure 29 is scaled to give the observed ratio of C IV equivalent width in 2016 to that in 2000–2001. This height, however, is about a factor of 4x lower than the increased flux in 2016 could potentially support via radiation pressure. Thus, gas at all radii is likely flowing upward and outward from the plane of the accretion disk as it is accelerated by the increased radiative flux. In addition, there is a substantial amount of gas at radii interior to 5 lt-days at high elevations that is now exposed to a much stronger ionizing flux. We suggest that this gas and the outflow induced by the increased ionizing flux is the source of the obscuring outflow observed by Mehdipour et al. (2017).

The changes we have observed in the structure of the BLR in NGC 3783, and perhaps in the mechanisms driving these changes, are similar to the more extreme variability seen in "changing-look" AGN. These AGN at their most extreme appear to change from Type 1, with bright, typical BLRs, to Type 2, with almost no remaining observational trace of the BLR. Examples date back to the earliest studies of AGN (e.g., Mrk 6, Khachikian & Weedman 1971) and NGC 4151 (Penston & Perez 1984). More recent, intensively studied examples include Mrk 590 (Denney et al. 2014; Mathur et al. 2018) and HE1136-2304 (Zetzl et al. 2018). In such objects, the continuum luminosity varies by one to two orders of magnitude; in the low-luminosity states, the BLR can nearly completely disappear, the extreme version of the dimunition we observed in NGC 3783. In models of the BLR produced by disk-driven winds, the BLR is expected to completely disappear below a critical luminosity required to sustain the outflow (Elitzur & Ho 2009; Elitzur et al. 2014), producing an AGN that is a "true Type 2", where the BLR is not merely obscured, but completely absent. Elitzur & Ho (2009) cite a threshold for such a transition at a bolometric luminosity of $L_{bol} = 1.5 \times 10^{38}(M_{BH}/10^7 M_\odot)^{2/3}$ erg s$^{-1}$. For the black hole mass of $2.35 \times 10^7$ $M_\odot$ in NGC 3783, this threshold is far below the bolometric luminosity of $2.8 \times 10^{44}$ erg s$^{-1}$ (based on the spectral energy distributions of Mehdipour et al. 2017), so we would not expect such a drastic reconfiguration of the BLR.

Comprehensive surveys of candidates in the Sloan Digital Sky Survey (SDSS) reveal that 30–50% of quasars exhibit extreme variability characteristic of changing-look AGN that lead to dramatic changes in the BLR (MacLeod et al. 2016; Rumbaugh et al. 2018; MacLeod et al. 2018). These objects have systematically lower Eddington ratios (<10%), and are similar in luminosity and Eddington ratio to Seyfert 1s like NGC 3783 ($L_{bol}/L_{Edd} \sim 0.02$). Thus, detailed study of a less extreme event such as we have observed may offer some insights into the physics governing AGN classification in general. A crucial difference between the events in NGC 3783 and in the changing-look quasars is the appearance of heavy obscuration accompanying the return to normal luminosities in NGC 3783. This may imply that in changing-look objects that much of the material in the accretion disk and the accompanying gas that supplies the wind for the BLR may have been emptied from the system during the low-luminosity state. This would leave no excess material to be ejected as the obscuring outflow during the return to normal brightness in the changing-look AGN.

### 4.2. Impact on the Host Galaxy

A high velocity wind originating in or near the BLR in an AGN can potentially have a significant impact on the host galaxy since the kinetic luminosity of an outflow varies with velocity, v, as $v^3$. For a spherical shell moving at this velocity with a radius R, a total hydrogen column density $N_H$ and covering fraction $\Delta\Omega$, the mass flux and kinetic luminosity of the outflow are

$$\dot{M} = 4\pi\Delta\Omega R N_H \mu m_p v$$

$$\dot{E}_k = \frac{1}{2}\dot{M}v^2$$

where $m_p$ is the proton mass and $\mu = 1.4$ is the mean molecular weight. The properties of the obscurer in NGC 3783 suggest it might have sufficient kinetic luminosity to have an evolutionary impact on the host galaxy.

Mehdipour et al. (2017) derive a radial distance for the obscurer of 10 lt-days; the C IV emission line region has a reverberation radius of 3.8 lt-days (Reichert et al. 1994). For a central black hole mass of $M_{BH} = 2.35 \times 10^7$ $M_\odot$ (Bentz & Katz 2015), Keplerian velocities at 10 lt-days and 3.8 lt-days are 3500 km s$^{-1}$ and 5600 km s$^{-1}$, respectively. These are typical of the velocities of the deepest point in the UV absorption troughs of the obscurer

($-3000$ km s$^{-1}$), and their highest velocity extent from line center at $-6200$ km s$^{-1}$, which suggest that the kinematics of the obscurer are similar to those of the BLR. Assuming a covering fraction of $\Delta\Omega = 0.25$, these velocities yield kinetic luminosities ranging from $9.4 \times 10^{41}$ erg s$^{-1}$ to $3.8 \times 10^{42}$ erg s$^{-1}$. For the bolometric luminosity during our December 2016 observations of $2.8 \times 10^{44}$ erg s$^{-1}$ (Mehdipour et al. 2017), and an Eddington luminosity of $2.8 \times 10^{45}$ erg s$^{-1}$ (for $M_{BH} = 2.35 \times 10^7$ $M_\odot$), the kinetic luminosity corresponds to a range of 0.34% to 1.4% of bolometric, but only 0.03–0.14% of the Eddington luminosity. Even if this high-velocity outflow is persistent, these kinetic luminosities are not quite sufficient to have an evolutionary impact on the host galaxy, for which they generally must lie in the range of 0.5–5% (Di Matteo et al. 2005; Hopkins & Elvis 2010) of the AGN Eddington luminosity.

## 5. Conclusions

Our UV spectra of NGC 3783 obtained with *HST*/COS in simultaneity with *XMM-Newton* X-ray observations triggered with *Swift* by a soft X-ray obscuration event reveal that the obscurer is a fast, broad outflow similar in character to those recently discovered in NGC 5548 (Kaastra et al. 2014), Mrk 335 (Longinotti et al. 2013), and NGC 985 (Ebrero et al. 2016). The outflow extends from zero velocity to a maximum velocity of $-6200$ km s$^{-1}$, with a maximum depth at $-3000$ km s$^{-1}$, and a mean depth at $-2840$ km s$^{-1}$. The UV absorption is visible in Ly$\alpha$, N v, Si iv, and C iv, indicating a moderate level of ionization. The X-ray determined column density of $N_H = 2.3 \times 10^{23}$ cm$^{-2}$ together with the UV ion column densities yield an ionization parameter of $\log \xi = 1.84^{+0.4}_{-0.2}$ erg cm s$^{-1}$, similar to highly ionized portions of the broad-line region.

Even though NGC 3783 was in an historically high UV flux state, the intrinsic absorption lines exhibit depths and ionization states similar to the lowest flux states seen in the past. The appearance of deep troughs and low-ionization states like C iii demonstrate that despite the high UV continuum flux, the ionizing UV must be shadowed by the soft X-ray obscurer, similar to the behavior seen in NGC 5548 (Arav et al. 2015).

The broad emission line profiles in NGC 3783 changed dramatically as well. Despite the high UV continuum flux, the emission line fluxes are comparable to those seen with STIS in 2001, and moderate-width ($\sim 2800$ km s$^{-1}$) portions of the broad-line profile have disappeared. We suggest that the central portions of the broad line region have collapsed in an infall, triggering the brightening observed in the UV and X-ray, and also triggering the obscuring outflow. Our observations illustrate the value of simultaneous UV and X-ray spectral observations to understand the kinematics and physical properties of obscuring events.

*Acknowledgements.* This work is based on observations obtained with the NASA/ESA HST, and obtained from the Hubble Legacy Archive. This work was supported by NASA through a grant for HST program number 14481 from the Space Telescope Science Institute, which is operated by the Association of Universities for Research in Astronomy, Incorporated, under NASA contract NAS5-26555. We also used XMM-Newton, an ESA science mission with instruments and contributions directly funded by ESA Member States and the USA (NASA), the NuSTAR mission, a project led by the California Institute of Technology (Caltech), managed by the Jet Propulsion Laboratory (JPL) and funded by NASA, and data supplied by the UK Swift Science Data Centre at the University of Leicester. We thank the *XMM-Newton*, *NuSTAR*, and HST teams for scheduling our Target of Opportunity triggered observations. SRON is supported financially by NWO, the Netherlands Organization for Scientific Research. SB acknowledges financial support from the Italian Space Agency under grant ASI-INAF I/037/12/0, and n. 2017-14-H.O. EC is partially supported by the NWO-Vidi grant number 633.042.525. BDM acknowledges support from the European Union's Horizon 2020 research and innovation programme under the Marie Skłodowska-Curie grant agreement No. 665778 via the Polish National Science Center grant Polonez UMO-2016/21/P/ST9/04025. POP acknowledges support from the CNES and CNRS/PNHE. GP acknowledges support from the Bundesministerium für Wirtschaft und Technologie/Deutsches Zentrum für Luft- und Raumfahrt (BMWI/DLR, FKZ 50 OR 1604) and the Max Planck Society.

## References

Anderson, J. & Bedin, L. R. 2010, Publications of the Astronomical Society of the Pacific, 122, 1035
Arav, N., Chamberlain, C., Kriss, G. A., et al. 2015, A&A, 577, A37
Arav, N., Edmonds, D., Borguet, B., et al. 2012, A&A, 544, A33
Baskin, A. & Laor, A. 2018, MNRAS, 474, 1970
Bentz, M. C. & Katz, S. 2015, PASP, 127, 67
Bentz, M. C., Walsh, J. L., Barth, A. J., et al. 2010, ApJ, 716, 993
Blandford, R. D. & McKee, C. F. 1982, ApJ, 255, 419
Crenshaw, D. M., Kraemer, S. B., & George, I. M. 2003, ARAA, 41, 117
Crenshaw, D. M. et al. 2009, ApJ, 698, 281
Czerny, B. & Hryniewicz, K. 2011, A&A, 525, L8
Czerny, B., Li, Y.-R., Hryniewicz, K., et al. 2017, ApJ, 846, 154
De Rosa, G., Peterson, B. M., Ely, J., et al. 2015, ApJ, 806, 128
Denney, K. D., De Rosa, G., Croxall, K., et al. 2014, ApJ, 796, 134
Di Matteo, T. et al. 2005, Nature, 433, 604
Dunn, J. P., Jackson, B., Deo, R. P., et al. 2006, PASP, 118, 572
Ebrero, J., Kriss, G. A., Kaastra, J. S., & Ely, J. C. 2016, A&A, 586, A72
Elitzur, M. & Ho, L. C. 2009, ApJ, 701, L91
Elitzur, M., Ho, L. C., & Trump, J. R. 2014, MNRAS, 438, 3340
Faucher-Giguère, C.-A. & Quataert, E. 2012, MNRAS, 425, 605
Ferland, G. J., Chatzikos, M., Guzmán, F., et al. 2017, RMxAA, 53, 385
Ferrarese, L. & Merritt, D. 2000, ApJ, 539, L9
Fukumura, K., Kazanas, D., Contopoulos, I., & Behar, E. 2010, ApJ, 715, 636
Gabel, J. R., Crenshaw, D. M., Kraemer, S. B., et al. 2003a, ApJ, 583, 178
Gabel, J. R., Crenshaw, D. M., Kraemer, S. B., et al. 2003b, ApJ, 595, 120
Gabel, J. R., Kraemer, S. B., Crenshaw, D. M., et al. 2005, ApJ, 631, 741
Gebhardt, K. et al. 2000, ApJ, 539, L13
Gehrels, N., Chincarini, G., Giommi, P., et al. 2004, ApJ, 611, 1005
Goad, M. R., Korista, K. T., De Rosa, G., et al. 2016, ApJ, 824, 11
Green, J. C., Froning, C. S., Osterman, S., et al. 2012, ApJ, 744, 60
Grier, C. J., Peterson, B. M., Horne, K., et al. 2013, ApJ, 764, 47
Harrison, F. A., Craig, W. W., Christensen, F. E., et al. 2013, ApJ, 770, 103
Hopkins, P. F. & Elvis, M. 2010, MNRAS, 401, 7
Horne, K., Peterson, B. M., Collier, S. J., & Netzer, H. 2004, PASP, 116, 465
Jansen, F., Lumb, D., Altieri, B., et al. 2001, A&A, 365, L1
Kaastra, J. S., Kriss, G. A., Cappi, M., et al. 2014, Science, 345, 64
Kaastra, J. S., Mehdipour, M., Behar, E., et al. 2018, ArXiv e-prints, arXiv:1805.03538
Kaspi, S. et al. 2002, ApJ, 574, 643
Kaufer, A., Stahl, O., Tubbesing, S., et al. 1999, The Messenger, 95, 8
Khachikian, E. Y. & Weedman, D. W. 1971, ApJ, 164, L109
King, A. 2003, ApJ, 596, L27
Königl, A. & Kartje, J. F. 1994, ApJ, 434, 446
Kormendy, J. & Ho, L. C. 2013, ARAA, 51, 511
Kriss, G. 1994, Astronomical Data Analysis Software and Systems, 3, 437
Kriss, G. A., De Rosa, G., Ely, J., et al. 2018, ApJ, in preparation
Kriss, G. A. et al. 2011, A&A, 534, A41
Krolik, J. H., Horne, K., Kallman, T. R., et al. 1991, ApJ, 371, 541
Krolik, J. H. & Kriss, G. A. 1995, ApJ, 447, 512
Krolik, J. H. & Kriss, G. A. 2001, ApJ, 561, 684
Liu, G., Zakamska, N. L., & Greene, J. E. 2014, MNRAS, 442, 1303
Liu, G., Zakamska, N. L., Greene, J. E., Nesvadba, N. P. H., & Liu, X. 2013a, MNRAS, 430, 2327
Liu, G., Zakamska, N. L., Greene, J. E., Nesvadba, N. P. H., & Liu, X. 2013b, MNRAS, 436, 2576
Longinotti, A. L., Krongold, Y., Kriss, G. A., et al. 2013, ApJ, 766, 104
MacLeod, C. L., Green, P. J., Anderson, S. F., et al. 2018, ArXiv e-prints, arXiv:1810.00087
MacLeod, C. L., Ross, N. P., Lawrence, A., et al. 2016, MNRAS, 457, 389
Magorrian, J., Tremaine, S., Richstone, D., et al. 1998, AJ, 115, 2285
Markowitz, A. G., Krumpe, M., & Nikutta, R. 2014, MNRAS, 439, 1403
Mathur, S., Denney, K. D., Gupta, A., et al. 2018, ArXiv e-prints, arXiv:1810.06616
Mathur, S., Gupta, A., Page, K., et al. 2017, ApJ, 846, 55
Mehdipour, M., Kaastra, J. S., Kriss, G. A., et al. 2017, A&A, 607, A28
Murphy, E. M., Lockman, F. J., Laor, A., & Elvis, M. 1996, ApJS, 105, 369
Murray, N. & Chiang, J. 1995, ApJ, 454, L105
Murray, N. & Chiang, J. 1997, ApJ, 474, 91
Nardini, E., Reeves, J. N., Gofford, J., et al. 2015, Science, 347, 860
Netzer, H., Kaspi, S., Behar, E., et al. 2003, ApJ, 599, 933
Onken, C. A. & Peterson, B. M. 2002, ApJ, 572, 746

Osterbrock, D. E. & Ferland, G. J. 2006, Astrophysics of gaseous nebulae and active galactic nuclei (Mill Valley: University Science Books)
Ostriker, J. P., Choi, E., Ciotti, L., Novak, G. S., & Proga, D. 2010, ApJ, 722, 642
Pancoast, A., Brewer, B. J., & Treu, T. 2014a, MNRAS, 445, 3055
Pancoast, A., Brewer, B. J., Treu, T., et al. 2014b, MNRAS, 445, 3073
Penston, M. V. & Perez, E. 1984, MNRAS, 211, 33P
Peterson, B. M. 1993, PASP, 105, 247
Peterson, B. M. & Wandel, A. 1999, ApJ, 521, L95
Pounds, K. A., Reeves, J. N., King, A. R., et al. 2003, MNRAS, 345, 705
Proga, D., Stone, J. M., & Kallman, T. R. 2000, ApJ, 543, 686
Proga, D. & Waters, T. 2015, ApJ, 804, 137
Reeves, J. N., O'Brien, P. T., Braito, V., et al. 2009, ApJ, 701, 493
Reichert, G. A., Rodriguez-Pascual, P. M., Alloin, D., et al. 1994, ApJ, 425, 582
Rumbaugh, N., Shen, Y., Morganson, E., et al. 2018, ApJ, 854, 160
Savage, B. D. & Sembach, K. R. 1991, ApJ, 379, 245
Schlafly, E. F. & Finkbeiner, D. P. 2011, ApJ, 737, 103
Scott, A. E., Brandt, W. N., Behar, E., et al. 2014, ApJ, 797, 105
Silk, J. & Rees, M. J. 1998, A&A, 331, L1
Soker, N. 2010, MNRAS, 407, 2355
Stirpe, G. M., Winge, C., Altieri, B., et al. 1994, ApJ, 425, 609
Theureau, G., Bottinelli, L., Coudreau-Durand, N., et al. 1998, A&AS, 130, 333
Thompson, T. A., Fabian, A. C., Quataert, E., & Murray, N. 2015, MNRAS, 449, 147
Tombesi, F. et al. 2010, A&A, 521, A57
Woodgate, B. E., Kimble, R. A., Bowers, C. W., et al. 1998, PASP, 110, 1183
Zetzl, M., Kollatschny, W., Ochmann, M. W., et al. 2018, A&A, 618, A83
Zubovas, K. & Nayakshin, S. 2014, MNRAS, 440, 2625

**Table 7.** Emission-Line Parameters for the COS 2011 and COS 2013 Spectra of NGC 3783

| | | COS 2011 | | | COS 2013 | | |
|---|---|---|---|---|---|---|---|
| Feature | $\lambda_0^a$ | Flux[b] | $v_{sys}^c$ | FWHM[d] | Flux[b] | $v_{sys}^c$ | FWHM[d] |
| C III | 1176.01 | 1.1 ± 0.2 | −100 ± 80 | 1200 ± 180 | 1.5 ± 0.3 | 0 ± 50 | 1200 ± 260 |
| Ly$\alpha$ | 1215.67 | 110.0 ± 3.7 | −110 ± 20 | 800 ± 20 | 100.0 ± 3.1 | −40 ± 10 | 800 ± 20 |
| Ly$\alpha$ | 1215.67 | 150.0 ± 5.9 | 180 ± 20 | 2430 ± 30 | 170.0 ± 5.8 | 90 ± 10 | 2310 ± 10 |
| Ly$\alpha$ | 1215.67 | 260.0 ± 9.3 | 890 ± 60 | 5190 ± 60 | 77.0 ± 3.9 | 1760 ± 40 | 6070 ± 50 |
| Ly$\alpha$ | 1215.67 | 230.0 ± 7.6 | −1160 ± 60 | 14870 ± 50 | 160.0 ± 5.3 | 200 ± 20 | 10590 ± 30 |
| N V blue | 1238.82 | 5.1 ± 0.3 | −30 ± 30 | 770 ± 80 | 7.4 ± 0.3 | −30 ± 10 | 770 ± 20 |
| N V red | 1242.80 | 5.1 ± 0.3 | −30 ± 30 | 770 ± 80 | 7.4 ± 0.3 | −30 ± 10 | 770 ± 20 |
| N V blue | 1238.82 | 6.0 ± 0.4 | 1080 ± 20 | 4240 ± 60 | 11.0 ± 0.5 | 580 ± 20 | 3690 ± 20 |
| N V red | 1242.80 | 6.0 ± 0.4 | 1080 ± 20 | 4240 ± 60 | 11.0 ± 0.5 | 580 ± 20 | 3690 ± 20 |
| N V | 1240.89 | 89.0 ± 3.0 | 480 ± 20 | 7270 ± 60 | 2.8 ± 0.4 | 450 ± 930 | 13100 ± 720 |
| S II | 1260.42 | 1.1 ± 0.5 | −150 ± 20 | 1600 ± 40 | 6.4 ± 0.4 | −150 ± 30 | 2460 ± 30 |
| O I+S II | 1304.46 | 11.0 ± 0.8 | 220 ± 20 | 2880 ± 100 | 11.0 ± 0.4 | 220 ± 20 | 2920 ± 30 |
| C II | 1334.53 | 4.3 ± 0.4 | 960 ± 50 | 2880 ± 100 | 4.0 ± 0.2 | 110 ± 30 | 2920 ± 30 |
| S IV blue | 1393.76 | 4.3 ± 0.4 | −280 ± 30 | 1310 ± 100 | 3.6 ± 0.2 | −70 ± 50 | 1260 ± 30 |
| S IV red | 1402.77 | 4.3 ± 0.4 | −510 ± 90 | 1310 ± 20 | 3.6 ± 0.2 | −70 ± 50 | 1260 ± 30 |
| S IV blue | 1393.76 | 19.0 ± 0.6 | 1060 ± 20 | 4740 ± 50 | 23.0 ± 1.3 | −120 ± 10 | 5920 ± 100 |
| S IV red | 1402.77 | 19.0 ± 0.6 | 1060 ± 20 | 4740 ± 50 | 23.0 ± 1.3 | −120 ± 10 | 5920 ± 100 |
| S IV | 1398.19 | 42.0 ± 1.4 | −360 ± 50 | 10850 ± 50 | 15.0 ± 1.2 | −3060 ± 70 | 17800 ± 50 |
| O IV] | 1401.16 | 1.8 ± 0.1 | 700 ± 40 | 1400 ± 130 | 2.1 ± 0.3 | 900 ± 40 | 1260 ± 10 |
| O IV] | 1401.16 | 11.0 ± 0.6 | 700 ± 40 | 4740 ± 20 | 1.9 ± 0.4 | 900 ± 40 | 5920 ± 10 |
| N IV] | 1486.50 | 0.0 ± 0.5 | 10 ± 30 | 5000 ± 190 | 0.7 ± 0.4 | 10 ± 20 | 500 ± 20 |
| N IV] | 1486.50 | 12.0 ± 0.5 | −260 ± 20 | 2590 ± 60 | 9.5 ± 0.4 | −260 ± 10 | 2590 ± 70 |
| C IV blue | 1548.19 | 40.0 ± 1.5 | −60 ± 20 | 940 ± 20 | 37.0 ± 1.6 | −60 ± 20 | 940 ± 10 |
| C IV red | 1550.77 | 40.0 ± 1.5 | −60 ± 20 | 940 ± 20 | 37.0 ± 1.6 | −60 ± 20 | 940 ± 10 |
| C IV blue | 1548.19 | 7.9 ± 0.8 | 300 ± 80 | 2840 ± 50 | 22.0 ± 1.6 | 500 ± 30 | 1390 ± 70 |
| C IV red | 1550.77 | 7.9 ± 0.8 | 300 ± 80 | 2840 ± 50 | 22.0 ± 1.6 | 500 ± 30 | 1390 ± 70 |
| C IV blue | 1548.19 | 140.0 ± 4.7 | 500 ± 20 | 4580 ± 20 | 68.0 ± 2.3 | −620 ± 30 | 5030 ± 40 |
| C IV red | 1550.77 | 140.0 ± 4.7 | 500 ± 20 | 4580 ± 20 | 68.0 ± 2.3 | −620 ± 30 | 5030 ± 40 |
| C IV | 1549.48 | 300.0 ± 10.0 | −430 ± 20 | 9840 ± 30 | 250.0 ± 7.9 | −140 ± 10 | 9220 ± 20 |
| He II | 1640.45 | 9.1 ± 0.6 | −80 ± 40 | 790 ± 50 | 6.9 ± 0.3 | 90 ± 20 | 790 ± 40 |
| He II | 1640.45 | 15.0 ± 0.6 | 840 ± 90 | 3250 ± 30 | 19.0 ± 1.1 | −110 ± 30 | 3450 ± 120 |
| He II | 1640.45 | 98.0 ± 3.0 | −120 ± 20 | 11080 ± 30 | 39.0 ± 1.9 | −5330 ± 40 | 23200 ± 660 |
| O III] | 1660.81 | 5.5 ± 0.3 | −160 ± 20 | 1200 ± 20 | 3.5 ± 0.4 | −160 ± 20 | 2790 ± 60 |
| O III] | 1666.15 | 6.5 ± 0.3 | −160 ± 20 | 1200 ± 20 | 15.0 ± 0.7 | −160 ± 10 | 2790 ± 60 |
| N III] | 1750.00 | 13.0 ± 0.4 | 0 ± 30 | 3270 ± 20 | 15.0 ± 0.5 | 0 ± 40 | 3270 ± 30 |

**Notes.**

[a] Vacuum rest wavelength of the spectral feature (Å).

[b] Integrated flux in units of $10^{-14}$ erg cm$^{-2}$ s$^{-1}$.

[c] Velocity (in km s$^{-1}$) relative to a systemic redshift of z = 0.00973 (Theureau et al. 1998).

[d] Full-width at half-maximum (km s$^{-1}$).